Funded by the European Union

Funded by the European Union under grant agreement No 101138341. Views and opinions expressed are however those of the author only and do not necessarily reflect those of the European Union. Neither the European Union nor the granting authority can be held responsible for them.

COMPARATIVE ANALYSIS OF HYBRID MACHINE TOPOLOGIES IN ENERGY CONVERSION MACHINES

Lappeenranta-Lahti University of Technology LUT

Mechanical Engineering, Master's thesis

2025

Pauli Pöppönen

Examiners: Professor, Jussi Sopanen

Tuhin Choudhury, D.Sc. (Tech.)

ABSTRACT

Lappeenranta-Lahti University of Technology LUT

LUT School of Energy Systems

Mechanical Engineering

Pauli Pöppönen

Comparative analysis of hybrid machine topologies in energy conversion machines

Master's thesis

2025

62 pages, 26 figures, 12 tables and 0 appendices

Examiners: Professor, Jussi Sopanen

Tuhin Choudhury, D.Sc. (Tech.)

Keywords: Active Magnetic Bearing, Design Comparison, Gas Turbine, Megawatt Scale, Modular Shaft, Rotordynamics, Turbomachinery

The growing demand for high-efficiency megawatt-scale power conversion systems raises the question of optimal machine topology. While sub-megawatt systems are typically integrated turbogenerators, larger systems often use separate turbine–generator units. A hybrid concept introduces a third radial bearing and flexible coupling, integrating the turbine shaft into the generator structure to combine compactness with rotor-dynamic benefits.

This study compares the dynamic behavior of this three-bearing configuration with a conventional two-bearing configuration. Five initial shaft layouts were analyzed for design, critical speeds, controllability, and vibration response under unbalance excitation. The results indicate that a layout with all process stages on a single extension shaft offers reduced vibration and easier crossing of critical speeds, with the second forward-whirl mode positioned far beyond the operational range. These findings highlight the potential of 3-AMB systems to improve modularity and dynamic stability in megawatt-scale turbomachinery.

TIIVISTELMÄ

Lappeenrannan–Lahden teknillinen yliopisto LUT

LUT Energiajärjestelmät

Konetekniikka

Pauli Pöppönen

Hybridikonetopologioiden vertaileva analyysi energianmuunnoskoneissa

Diplomityö

2025

62 sivua, 26 kuvaa, 12 taulukkoa ja 0 liitettä

Tarkastajat: Professori, Jussi Sopanen

Tuhin Choudhury, Tekniikan tohtori

Avainsanat: Aktiivi magneettilaakeri, suunnittelu vertailu, kaasuturbiini, megawattimittakaava, modulaarinen akseli, rootoridynamiikka, turbiinikoneisto

Kasvava tarve korkean hyötysuhteen megawattitason tehonmuunnosjärjestelmille herättää kysymyksen optimaalisen konfiguraation valinnasta. Alle megawatin järjestelmät toteutetaan tyypillisesti integroituna turbogeneraattorina, kun taas suuremmat järjestelmät koostuvat usein erillisistä turbiini–generaattoriyksiköistä. Hybridikonsepti yhdistää turbiinin akselin generaattorirakenteeseen kolmannen radiaalilaakerin ja joustavan liittimen avulla, mikä yhdistää kompaktin rakenteen ja erillisten yksiköiden roottoridynaamiset edut.

Tässä tutkimuksessa verrataan kolmen laakerin konfiguraation dynaamista käyttäytymistä perinteiseen kahden laakerin ratkaisuun. Viisi alustavaa akselikonfiguraatiota analysoitiin suunnittelun, valmistuksen, kriittisten nopeuksien, ohjattavuuden ja epätasapainosta johtuvan värähtelyvasteen osalta. Tulokset osoittavat, että konfiguraation, jossa kaikki prosessivaiheet sijaitsevat yhdellä jatkoakselilla, tarjoaa pienemmät värähtelytasot ja helpomman kriittisten nopeuksien ylityksen, kun toinen eteenpäin pyörivä taivutusmoodi sijaitsee selvästi käyttöalueen yläpuolella. Nämä havainnot korostavat 3-AMB-järjestelmien potentiaalia parantaa modulaarisuutta ja dynaamista vakautta megawattitason turbokoneissa.

ACKNOWLEDGEMENTS

This work was supported by funding from the European Union's Horizon Europe research and innovation programme under grant agreement No 101138341 (MARPOWER - Efficient zero-emissions gas turbine POWER system for MARitime transport).

First, I would like to thank Jussi Sopanen and Tuhin Choudhury for being patient and for this great opportunity to work with them. I have learned a lot working with them in the Machine Dynamics lab.

Also, I would like to thank Juuso Narsakka for being a great help on this journey by providing good insights. I also thank Gyan Ranjan for answering my questions when needed.

Lastly, I thank my significant other who has supported me, kept me going, and made my day.

Pauli Pöppönen

Pauli Pöppönen

Lappeenranta 17.12.2025

ABBREVIATIONS

Roman characters

$\mathbf{A}$	System matrix	
a	Real part	
$\mathbf{C}$	Damping matrix	Ns/m
$F_Y,\ F_Z$	Centrifugal force components	N
$\mathbf{f}$	Force vector	N
$\mathbf{G}$	Gyroscopic matrix	kgm^2/s
I_d	Diametral moment of inertia	kgm^2
I_p	Polar moment of inertia	kgm^2
$\mathbf{K}$	Stiffness matrix	N/m
$\mathbf{K}^*$	Stiffness matrix without bearing	N/m
$\mathbf{K}_a$	Displacement stiffness matrix	Nm/rad
$\mathbf{K}_i$	Current stiffness matrix	Nm/rad
$\mathbf{K}_R$	Rotational stiffness matrix	Nm/rad
$\mathbf{K}_t$	Isotropic translational stiffness matrix	N/m
$\mathbf{i}_c$	Control current applied	A
j	Imaginary unit	
l	Length	m
$\mathbf{M}$	Mass matrix	kg
m_d	Mass of disk	kg
m_u	Unbalance mass	kg
$\mathbf{q}$	Displacement vector	m
$\dot{\mathbf{q}}$	Velocity vector	m/s
$\ddot{\mathbf{q}}$	Acceleration vector	m/s^2
r	radial distance	m
$\mathbf{r}_a$	Displacement of node a	m
t	Time	s

x	Displacement on axis x	m
$\dot{x}$	Velocity on axis x	m/s
$\ddot{x}$	Acceleration on axis x	m/s^2
y	State vector	
z	Vector of constants	N

Greek characters

β	Imaginary part	m
$\dot{\theta}_x$,	Angular velosity on axis x	rad/s
$\dot{\theta}_y$,	Angular velosity on axis y	rad/s
$\dot{\theta}_z$	Angular velosity on axis z	rad/s
λ	Eigen Value	
ν	Poisson's ratio	
φ_x	Rotation on axis x	rad
φ_y	Rotation on axis y	rad
φ_z	Rotation on axis z	rad
Ω	Angular velocity	rad/s

Subscripts

a	Specified node
i	ith mode
n	nth node
n	Number of natural frequencies
$1,\ 2,\ 3\ldots$	component number

Abbreviations

AAMB	Axial Active Magnetic Bearing
AMB	Active Magnetic Bearing
BW	backward whirling

Coup	coupling
CRB	Cylindrical Roller Bearing
DCM	Direct Current Machine
DOF	Decrees Of Freedom
EOM	Equation of Motion
FEM	Finite Element Method
FW	forward whirling
Gen	generator
HPC	High Pressure Compressor
HPT	High Pressure Turbine
HS	high-speed
IM	Induction Machine
PM	Permanent Magnet
PMB	Passive Magnetic Bearing
PMSM	Permanent Magnet Synchronous Machine
RAMB	Radial Active Magnetic Bearing
REB	Rolling-Element Bearing
RoBeDyn	Rotor Bearing Dynamics
rpm	revolutions per minute
SM	Synchronous Machine
SPM	Surface Permanent Magnet
SRB	Spherical Roller Bearing
SRM	Synchronous Reluctance Machine
TDB	Touchdown bearing

Table of contents

DECLARATIONS

Turnitin
The originality of this thesis has been reviewed with the Turnitin similarity checking service.

AI usage
The author of the thesis, Pauli Pöppönen, used the following AI-tools during the preparation of the thesis:

1. Scopus AI
    a. Purpose of use: To explore how Scopus AI works and search the literature and authors related concepts for to thesis.
    b. Explanation of the use of the tool: At the beginning of the thesis, Scopus AI was used to understand keywords relevant to the literature used.
2. ChatGPT
    a. Purpose of use: Grammar checking and to teach and guide how to write text more academically.
    b. Explanation of the use of the tool: At the beginning of the thesis, ChatGPT was used to grammar check, revise the written text, and provide suggestions for improving academic tone.
3. Mirosoft CoPilot
    a. Purpose of use: Revise text, color hex codes, teaching to write academic text.
    b. Explanation of the use of the tool: At middle of the writing thesis changed to Microsoft CoPilot primarily for rewrite text, reducing spoken language thus improving academic style. At the end of the writing thesis was used to provide hex color values.
4. Overleaf Writefull
    a. Purpose of use: Revise the text.
    b. Explanation of the use of the tool: At the end of the writing used to check minor errors and check the flow of written text.

Responsibility
The author, Pauli Pöppönen, takes full responsibility for the content of this thesis and has reviewed and edited the content generated by the possible use of AI tools.

1 Introduction

Rotating machines, particularly turbomachines are widely used to convert fluid energy into mechanical energy, or other way around. These machines play a crucial role in a variety of applications, including turbines, compressors, pumps, fans, and blowers. The first commercial use of turbomachines was in marine applications, followed by their adoption in power generation. (Rangwala, 2005, p. 3 - 12.) Many technological innovations in this field were initially developed for aerospace purposes and later adapted for other industries. A notable example is the modern gas turbine, which was originally designed as an aircraft engine. (Breeze, 2016, p. 32.)

Mechanical energy is quite often converted to or from electrical energy in these applications, making rotating machines integral to many industrial and power generation processes (Figure 1). For instance, turbines can convert mechanical energy from steam, water, or wind into electrical energy, which is then used to power homes, businesses, and industries. (Cengel & Cimbala, 2014, p. 833.)

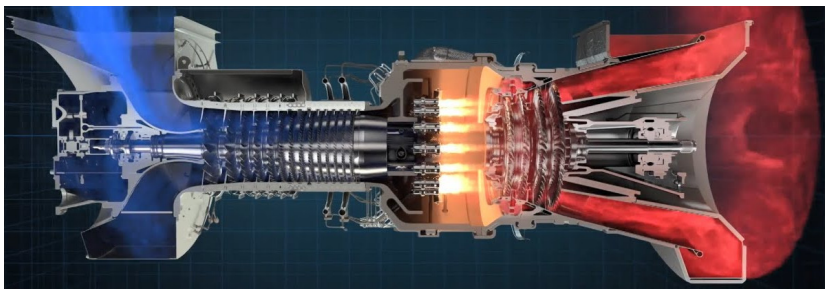

Figure 1: Gas turbine (Solar Turbines, 2019.)

Conversely, electric motors convert electrical energy into mechanical energy to drive pumps, fans, compressors, and other machinery (Kutz, 2014, p. 857). This bidirectional energy conversion is essential for maintaining the efficiency and functionality of various systems. Figure 2 shows conventional design of gas turbine.

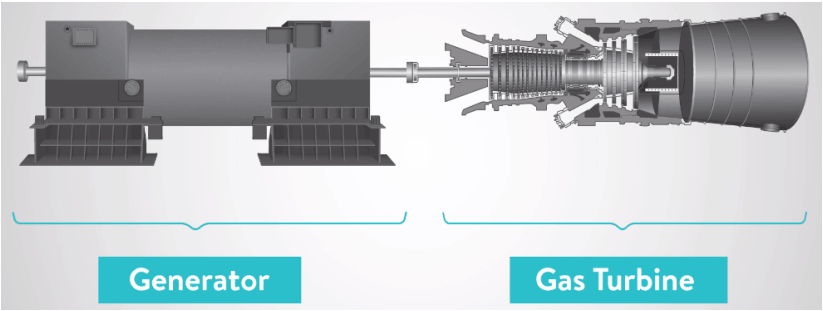

Figure 2: Generator and Gas turbine (Sultan, 2019)

When high-speeds (HSs) are used on these machines these are highly desirable and sought after. HS electric machines are applications where operational speeds exceeds $10,000$ revolutions per minute (rpm) and dynamic speed exceeds rpm$\sqrt{kW} = 10^5$ (Van Millingen & Van Millingen, 1991; Gerada et al., 2013). This increased rotational speed and increased power density is appealing direction for development, as these machines can be physically smaller than other more traditional options. Kurvinen et al. (2019) Interest in higher power-density and energy-efficiency combined with electrifying the future transport methods has driven research towards high-speed electric technology. (Gerada et al., 2013.)

There are several applications of HS electric machines. Figure 3 shows some of the key applications in terms of their nominal power and speed. In Figure 3, the green line signifies lower bound of HS electric machines in terms of power and speed. Another way to classify HS machines is by high speed-index which is product of nominal power and nominal speed seen as $\text{HS}_{id} = \text{krpm} \times \text{MW}$. (Moghaddam, 2014.)

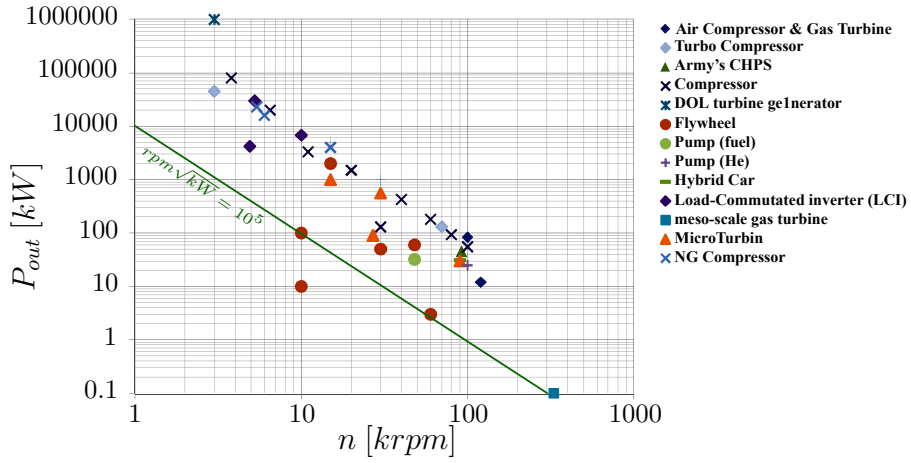

Figure 3: Power (kW) vs rotation speed (krpm) chart showing the key application areas of high speed machines (Van Millingen & Van Millingen, 1991; Moghaddam, 2014).

There are many design choices on HS electric machines which effects on speeds and powers. These design choices differentiate types of electrical machines that are used, and all these have trade-offs between requirements and level of complexities. Moghaddam (2014) listed the following as some of most common types of electric machines: Direct Current Machine (DCM), Induction Machine (IM), Permanent Magnet (PM), Surface Permanent Magnet (SPM), Synchronous Machine (SM), Synchronous Reluctance Machine (SRM).

1.1 Research Background

Integrated gas turbine as HS electric generator have been chosen as the focus on this study, as these machines are highly desired of their high efficiency. Also as these operational speeds increases to high speeds (Figure 3) its power density also increases which makes these more effective. Overal efficiency of gas turbines can reach at power plants to 60% in operation time. (Van Millingen & Van Millingen, 1991; Breeze, 2016)

1.1.1 Generator topologies

HS electrical machines have been researched and used many years as these compact, efficient, and high power density machines are good solutions on various industries. There are different rotor topologies (Figure 4) on use at HS applications that gives advantages or limitations on their specific cases. Figure 4(a) - (d) shows the cross section of rotor topologies used in IMs. This solid rotor topology provides robustness and such commonly used on many applications. Figure 4(e) - (g) are used in Permanent Magnet Synchronous Machine (PMSM). For both of these machines topology is selected carefully to provide enough structural integrity and at the same time, it should provide enough magnetic flux. (Gerada et al., 2013; Uzhegov, Kurvinen & Pyrhönen, 2014)

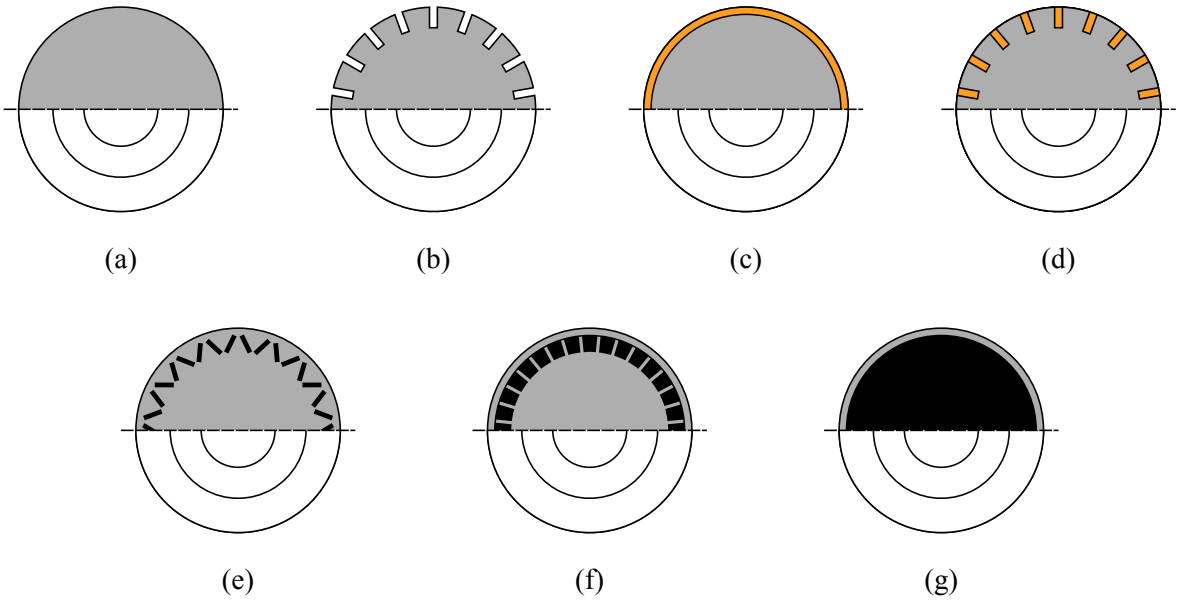

Figure 4: Different topologies that solid rotor can have, a) solid smooth rotor, b) slitted solid rotor, c) coated solid rotor, d) caged solid rotor, e) Multiple-pole internal permanent magnet, f) Two or multiple pole surface permanent magnet with retaining sleeve, g) Two-pole full cylindrical magnet with retaining sleeve (Gerada et al., 2013; Uzhegov, Kurvinen & Pyrhönen, 2014)

These machines are collaborative design efforts of electrical, mechanical, and material design. High-speed brings challenges to rotor design related to mechanical stresses, critical speeds, cooling, and specific power output. As these HS machines are used in many industries, these requirements are constantly evolving as well. Furthermore there is

increased need for oil free applications which adds on these challenges. In this regard, magnetic bearings have been used successfully, which have leaded increase to safety, efficiency and availability, these have reduced operation and maintenance costs such machines. (Gerada et al., 2013)

As these HS machines are more common and widely used, demands on these machines grow so more powerful machines are needed. These so called megawatt range machines brings some extra challenges on reliable design and manufacturing. These challenges are related to size of rotor, size of active part, and its different topologies it can have each having different challenges. On manufacturing there is some standards that help with these but when size increases tolerances increases too and that can make assembly of these machines challenging, and size could require specialized manufacturing machines. HS machines that have copper on active part needs to take account high temperatures and high rotational speeds, because coppers lower yield strength. At operation startup on HS is often gone over at least one critical frequency, this is needed to keep in mind, and some times is one of limiting factors. (Kurvinen et al., 2019; Tenconi, Vaschetto & Vigliani, 2014)

1.1.2 Bearings

Rolling-Element Bearings (REBs) are mainly made on three different elements, which are inner ring, outer ring, rolling elements, and usually cage that keeps rolling elements apart and guide them. These rolling elements are usually made from chrome alloy steel, and could be on many different shapes as balls, rollers, cones, or needles. There are many different subtypes, these subtypes includes Spherical Roller Bearing (SRB), Cylindrical Roller Bearing (CRB), and many others. These REB are used usually as Touchdown bearing (TDB) with magnetic bearings to give safety on possible problem situation, to give support and to help keeping machines on working condition.

There is also fluid bearings, that uses thin layer of liquid or gas to reduce sliding friction with rotating element. These are hydrostatic or hydrodynamic bearings, and require minimal maintenance and also provide a long service life. Hydrostatic bearing said to be invented 1852 by Girard, wo used these on railway propulsion (Rowe, 2012).

Magnetic bearings related to other types are quite new invention, as one of the first suggestion to use electromagnets are from 1937 (Maslen et al., 2009.). There is two main types of magnetic bearings, which are Active Magnetic Bearing (AMB) and Passive Magnetic Bearing (PMB). Main idea on these is to use magnetic levitation to support moving parts (Figure 5a), this does not require any contact thus having low friction and minimal wear. PMB uses permanent magnets and does not need any input power and are limited by their own capability. AMB uses electromagnets which requires power input and control system (Figure 5b), giving these more stable placement when used correctly related to PMB. On Figure 5b are two types of AMBs first Radial Active Magnetic Bearing (RAMB) and second is Axial Active Magnetic Bearing (AAMB).

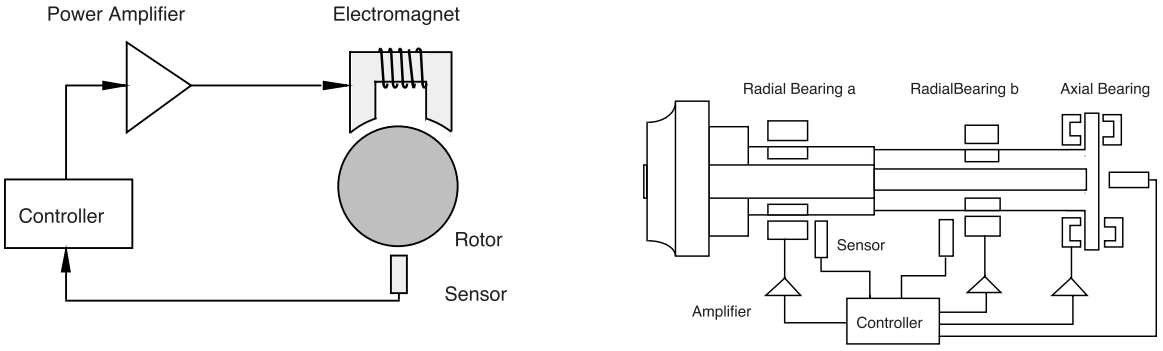

Figure 5: AMB working principle schematics a) the function principle of the active electromagnetic suspension, b) suspension of a rotor in one plane. (Maslen et al., 2009 p.2 - 3.)

AMBs stability have been tested on multiple times on different applications. As Zhao et al. (2024) made test of flywheel AMBs stability on a rotating platform, where they measured gyroscopic effects, magnetic forces, and rotational dynamics and these interactions. Trough modeling and experimental test study shows AMBs effectiveness to stabilize and suppress negative effects on flywheel during high-speeds, up to 31200 rpm.

On article Uzhegov et al. (2017) discusses challenges of AMBs and provides case studies on a 120 kW IM and a 200 kW PM machine, both designed to operate with AMBs in compressor applications. These case studies shows how the AMBs allows for HS operation while maintaining rotor stability without the physical contact of bearing systems. Overall,

the use of AMBs in conjunction with HS electrical machines provides a solution that enhances the performance of compressors, offering a low-maintenance, high-speed, and efficient alternative to traditional systems.

Smirnov et al. (2017) talks a multi-objective optimization approach that refines both the AMB and machine components simultaneously, ensuring stability, thermal management, and performance. Balancing these elements, the AMBs are able to precisely control and stabilize the rotor. The study underscores that AMBs are a critical factor in achieving the optimal performance and reliability of high-speed electrical machines.

Kang & Yoon (2005) discussed the application of an active magnetic bearing (AMB) system to stabilize the elevation axis of an electro-optical sight on a moving vehicle. They aimed to maintain the elevation axis in an air-gap between magnetic bearing stators while the vehicle is in motion. To reduce disturbances caused by base motion, they proposed an acceleration feedforward compensator designed using the filtered least mean square (FXLMS) algorithm. Due to the sensitivity of disturbance compensation performance to model accuracy, an experimental feedforward compensator was developed. The feasibility of this technique was demonstrated through experiments, showing that the feedforward compensation effectively reduces the response to base motion.

1.1.3 Design configuration

On gas turbine generators and conversion usual configuration on 2-RAMB is Figure 6a, this configuration is small on its design and makes it desirable on places where installation place is one of the required variables. In this study, the 3-RAMB configuration (Figure 6b) is compared to this 2-RAMB configuration.

Most studies have conducted research on 2-RAMB (Figure 6a or similar), while only few have proposed 3-RAMB (Figure 6b or similar). Most of these 3-RAMB cases that on literature are using coupling methods for rotor extensions. There is some benefits on thermal protection, assembly, maintenance, larger operation range and challenges on these as complex calculations, increased vibration amplitude, larger repetitive loads on extension end. (Narsakka et al., 2023; Ranjan et al., 2023; Choudhury et al., 2024)

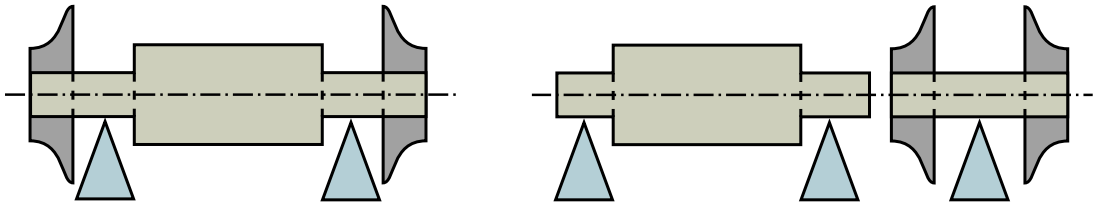

Figure 6: Two configurations a) 2-AMB more common, b) 3-AMB on inspection at this study

Derakhshandeh (2023) found on her thesis that integrated system was most suited on her case, but cases where extension and coupling are used with different bearings gyroscopic effect where lower that integrated system. On her study is easy to see how these extension shafts adds more length whole rotor. Even when these AMBs are low maintenance, oil free, better damping properties, and control is easier, this extra controller can make the design complex. These differences on different cases are needed to compered to get full understanding how these cases behave.

Bidaut, Somaini & Ruguê (2019) used on their research 3-RAMB rotor desing and found out, AMB equipped centrifugal compressors differ significantly from conventional oil-film bearing systems in terms of stability requirements. AMBs have lower load capacity and stiffness, making rotordynamic stability a more critical concern. While conventional systems primarily focus on low-frequency stability analysis, AMB systems require evaluation across the full frequency range due to their dynamic characteristics. Additionally, traditional stability assessment methods for oil-bearing machines are insufficient for AMB compressors, which demand more comprehensive analyses, including radial force variation and closed-loop transfer functions. These differences highlight the unique technical challenges of AMB-equipped compressors.

1.2 Research problem and questions

The design and dynamic analysis of megawatt-scale HS machines for gas turbine at moving platform applications are not widely researched area, particularly in the context of 3-RAMB

supported systems compared to conventional 2-RAMB configurations. The primary focus of this research is on dynamic modeling and analysis, with the following key aspects:

- How does the placement of components in a 3-RAMB system affect mechanical design compared to a 2-RAMB system?
- What are the differences in rotordynamics between 3-RAMB and 2-RAMB configurations?
- In which cases does the 3-RAMB layout provide measurable benefits over the 2-RAMB reference case?

The goal is to provide a comprehensive understanding of the dynamic behavior differences between 3-RAMB and 2-RAMB supported gas turbines in megawatt-scale applications on moving platform, ultimately informing differences on critical speed, load capacity, and gyroscopic effect.

1.2.1 Objectives

The objective of this study is to evaluate gas turbine support benefits of 3-RAMB configuration compared to a 2-RAMB.The goal is to find which cases 3-RAMB offers advantages and how close to 2-RAMB these cases are. This can be done on using different aspects, like mechanical design, rotordynamics, weight, size and etc. on mind.

- Conduct rotordynamic analyses for each configuration to assess critical speeds, mode shapes, and unbalance.
- Perform a preliminary design analysis to understand the mechanical implications of component placement.
- Provide recommendations for rotor AMB layout based on dynamic performance and design constraints.

1.2.2 Scope

As this research includes the analysis of the rotordynamics of gas turbine shaft system and a comparison between the system supported by 2 RAMBs, versus 3 RAMBs. When critical speed, load capacity and gyroscopic effect are under investigation.

On this research of 3-RAMB vs 2-RAMB gas turbines will not cover some areas. It does not look at fluid dynamics or do detailed calculations. The study will not go deep into controller design or cooling systems. It also will not examine the electro-magnetics of AMBs or generators. Lastly, it will not deal with regulations for gas turbines. The focus is on comparing overall performance, design, between the different AMB layouts.

2 Rotor Dynamics Modeling and Analysis Methods

As rotating machines have a variety of elements, for example shafts, disks, bearings, seals, coils, and gears. These components are influenced by various factors, including fluid forces, lubrication effects, and electromagnetic interactions. This reason rotors have high possibility to generate vibrations. These vibrations causes problems for rotating machinery, and risk of machine breaking increases. To reduce these vibrations on normal working conditions, analysis of design is needed to avoid these unwanted vibrations. (Matsushita et al., 2017, p. 6.)

Rotordynamics aims to establish methodologies for reduction/supression of vibrations. Understanding these methodologies and the causes of vibration in rotating machinery, including excitation forces, mechanisms, and the natural frequencies, enables to optimization of the design, operation, and maintenance of machine. (Matsushita et al., 2017, p. 6 - 7.) In Figure 7 is shown example case on 3-RAMB model and different sections that is taken account for design and calculations.

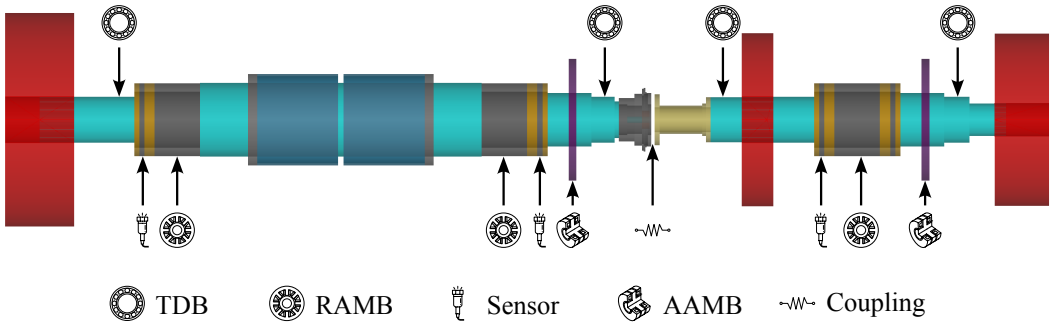

Figure 7: Rotor model on case 3-RAMB

There is frequently encountered rotor vibration modes that are categorized as follows bending, torsional, longitudinal vibration of the shaft, and vibration of rotating structure. On bending vibration of the shaft, shaft whirls in its rotation plane while it maintains its deflection mode that varies along the axis. This whirling shaft mode is measured as it being

rigid and/or flexible. Many problems on shaft, caused by vibrations can be described by these bending modes. On other hand torsional vibration of the shaft arises when vibrations of each part are twisted by rotational axis. Torsional vibration occurrence is small compared to bending vibration at rotating machinery. Reciprocating, gears, electromagnetic forces, or torque of the load may cause torsional vibrations. Longitudinal vibrations of the shaft is usually small or not appear because stiffness of the shaft. There have been cases where collision with static part and thrust bearing dynamic load excites this mode. Vibration of rotating structure is important to take account when designing actual geometries of example impellers or blades. These bending vibrations requires detailed calculations of natural frequencies and prediction of resonance amplitudes. (Matsushita et al., 2017, p. 8.)

2.1 Mathematical model of rotor

To make mathematical models these complex machines simplification is needed, this simplification depends on practical experience, theoretical knowledge, and engineering intuition (Matsushita et al., 2017, p. 10.). In rotor dynamics, the Equation of Motion (EOM) are crucial for modeling. These equations describe the behavior of the system using variables that are functions of time. These equations can be described using variables, that are functions of time. (Chen & Gunter, 2001, p. 1.)

$$\mathbf{M}\ddot{\mathbf{q}}(t) + (\Omega\mathbf{G} + \mathbf{C})\dot{\mathbf{q}}(t) + \mathbf{K}\mathbf{q}(t) = \mathbf{f}(t) \tag{2.1}$$

In Equation 2.1, **M** is mass matrix, **G** is gyroscopic matrix and **C** damping matrix **K** is general stiffness matrix. Angular velocity is Ω, $\mathbf{q}$ is vector of generalized coordinates including displacements and rotations, $\dot{\mathbf{q}}$ is velocity matrix, and $\ddot{\mathbf{q}}$ is acceleration matrix. $\mathbf{f}$ is applied and system generated force vector. The minimum number of independent variables required for describe the motion of an system is known as the Decrees Of Freedom (DOF). (Chen & Gunter, 2001, p. 2 - 3.; Genta, 2007, p. 5.)

Mass matrix **M** represents the distribution of mass and inertia within the system. It is derived from the kinetic energy of the system and is typically a positive symmetric matrix.(Chen &

Gunter, 2001, p. 3.) For cylindrical elements in torsional vibration, it is sometimes assumed that the element's inertia is lumped at its two endpoints, with half of the inertia at each end. This diagonal mass matrix is referred to as the lumped mass matrix for the cylindrical element. (Chen & Gunter, 2001, 371 - 372.)

Damping matrix **C** takes account for energy dissipation in the system due to damping effects, which could be related to such as material properties or fluid interactions. (Chen & Gunter, 2001, p. 3.) For rotating elements at , the damping matrix must be assembled separately from the non-rotating ones. This results in two distinct matrices, one for rotating damping and another for non-rotating damping. (Genta, 2007, p. 102.)

Stiffness matrix **K** describes the elastic properties of system. It is derived from the potential energy stored in the system due to elastic deformation. The stiffness matrix can include terms that account for cross-coupled stiffness, which affects the system stability and vibration characteristics. (Chen & Gunter, 2001, p. 3.)

Gyroscopic matrix **G** represents the gyroscopic effects due to the rotation of the rotor. (Chen & Gunter, 2001, p. 3.) It is derived from the angular momentum of the system and is typically a skew-symmetric matrix. Since gyroscopic moments are proportional to angular velocities, they are often grouped with viscous damping terms in the equations of motion. However, unlike viscous damping, the gyroscopic matrix is a conservative force that does not dissipate energy. Due to the gyroscopic effect, each natural whirl frequency splits into two modes, forward whirl and backward whirl, when the rotor speed is non-zero. (Chen & Gunter, 2001, p. 92.)

2.1.1 Finite element method

The Finite Element Method (FEM) is a widely used technique in rotordynamics for modeling complex rotating machinery. FEM involves dividing a structure into smaller, manageable parts called finite elements. These elements can be of various types, such as beam elements, shell elements, plate elements, and solid elements. In rotordynamics, beam, mass, and spring elements are commonly used. (Genta, 2007, p. 156.)

Each finite element represents a small, deformable part of the structure with a limited number of DOF, replacing the infinite DOF of a continuous system. The displacement of a point within an element is approximated using shape functions, which are mathematical expressions that describe how the element deforms. These shape functions must meet specific conditions to ensure accurate modeling, such as being continuous and differentiable, and allowing for smooth deformation. (Genta, 2007, p. 156 - 157.)

The FEM approach simplifies the analysis of complex structures by converting continuous models into discrete models. This involves transforming physical models with partial differential equations into mathematical models with simultaneous differential equations. The resulting system of equations can then be solved to predict the dynamic behavior of the rotor system. (Genta, 2007, p. 156 - 157.)

2.1.2 Beam element

Rotors are often modeled using Timoshenko beam elements, which account for shear deformation, unlike Euler-Bernoulli beams. A simple Timoshenko beam element has two nodes at its ends and six degrees of freedom per node, representing a prismatic homogeneous beam with uncoupled axial, torsional, and flexural behavior Figure 8. Each cross-section has three displacement and three rotational degrees of freedom, resulting in a total of 12 degrees of freedom for the element. (Genta, 2007, p. 156 - 165.)

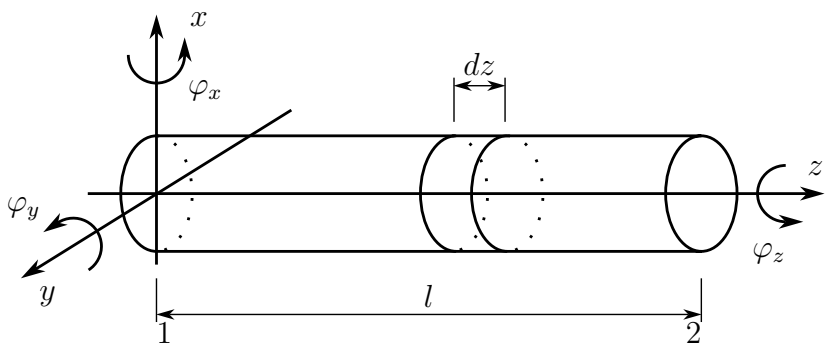

Figure 8: Simple Timoshenko beam element (modified from Genta, 2007, p. 160.)

To include shear deformation without encountering the locking problem—an overestimation of stiffness—specific shape functions are used. These functions depend on the non-dimensional coordinate $\varsigma = x/l$ and the parameter $\mathbf{\Phi}$, which approaches zero for an Euler-Bernoulli beam. The beam's properties in both planes are assumed equal, allowing for a simplified description of bending behavior. The total potential energy is computed by adding contributions from both bending and shear deformations, leading to the stiffness matrix. (Genta, 2007, p. 156 - 165.)

The kinetic energy of the beam is determined by considering it as a rigid body, accounting for both translational and rotational motion. The mass matrices for translational and rotational inertia are then defined, ensuring accurate representation of dynamic behavior. The consistent mass and gyroscopic matrices are derived, incorporating the effects of shape functions across the beam's length. (Genta, 2007, p. 156 - 165.)

A concentrated mass or rigid body at a node follows the same mass and gyroscopic matrix formulation as a rotor with four degrees of freedom. A spring element introduces localized stiffness between two nodes, such as shaft joints or linearized bearings, with distinct stiffness values for displacements and rotations. The equations of motion for an element are written relative to a local or element reference frame, determined by the element's features. (Genta, 2007, p. 156 - 165.)

2.1.3 Disc Element

As mentioned before disk elements are often used on rotor dynamics, these are usually impellers, fans, support masses, and mass dampers. This disk element on small vibrations can be divided on translational and rotational components within fixed reference frame Figure 9. (Chen & Gunter, 2001, p. 119.)

$$T = \frac{1}{2}m_d\left(\dot{x}^2 + \dot{y}^2\right) + \frac{1}{2}I_d\left(\dot{\theta}_x^2 + \dot{\theta}_y^2\right) + \frac{1}{2}\Omega I_p\left(\dot{\theta}_x^2\theta_y - \theta_x\dot{\theta}_y^2\right) + \frac{1}{2}\Omega^2 I_p \qquad (2.2)$$

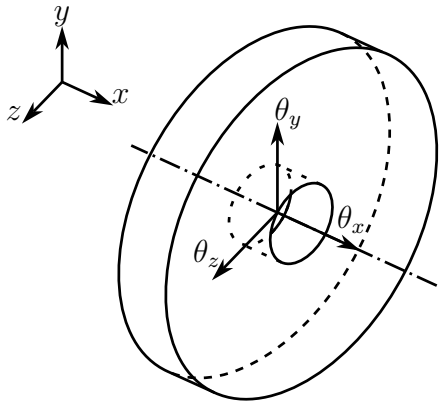

Figure 9: Disc element (modified from Chen & Gunter, 2001, p. 119.)

On Equation 2.2 m_d is mass of the disk, I_d is diametral (transverse) mass moment of inertia, I_p is polar mass moment of inertia. First term of equation accounts for translational kinetic energy, second term represents portion of the rotational kinetic energy. this is arising from the disk's rotational inertia and angular motion. These terms are always positive. Third term is also know as gyroscopic effect, it is linear within respect of generalized velocities and results from the gyroscopic moments. Depending on disk motion third term can be positive or negative. Fourth term is caused by pure spinning of the disk and does not depend on vibrational coordinates, and such can be ignored in the analysis of vibrations. (Chen & Gunter, 2001, p. 119 - 120.)

2.2 Couplings

For longer and extended rotors usually coupling is needed (Figure 10) to do and its often modeled as an elastic component between rotor beams as can be seen on Figure 10b as can bee seen beam element is disconnected to each other leaving a gap between two nodes here and coupling is modeled as elastic component. This coupling element contains $\mathbf{K}_T$ as isotropic translational stiffness and $\mathbf{K}_R$ as rotational stiffness between ends of rotors connecting ends. Couplins mass and inertia properties are usually lumped on ends of nodes (Figure 10b node_n and $\text{node}_{\text{n}+1}$). (Chen & Gunter, 2001, p. 170.)

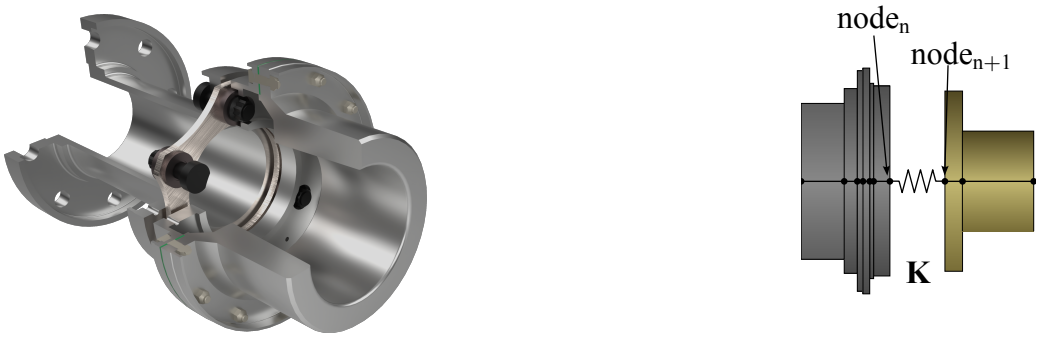

(a) (b)

Figure 10: Coupling figures a) model of half-Renk coupling on cutout can bee seen plate which is then modeled as this elastic component, b) coupling modeling as elastic component, coupling parts divided on rotor shaft ends and between those elastic component.

2.3 Active magnetic bearings

The performance of AMB in rotor dynamic systems is critically influenced by their force generation capacity, stiffness, and damping characteristics. These parameters determine the rotor's stability, critical speeds, and response to dynamic loads.

The force produced by an AMB is based on electromagnetic principles. Typically, radial AMBs are constructed using multiple magnetic poles arranged around the rotor. When current flows through the coils surrounding these poles, a magnetic field is generated, which pulls the rotor toward the center. The strength of this force depends on several factors, including the area of the magnetic poles, the number of coil turns, the current applied, and the size of the air gap between the rotor and the poles. (Maslen et al., 2009 p. 17 - 82.)

$$\mathbf{f}_a(t) = -\mathbf{K}_a\mathbf{r}_a + \mathbf{K}_i\mathbf{i}_c \tag{2.3}$$

For AMB support, Ranjan et al. (2023) (p. 192.) utilizes linearized AMB force model with differential driving mode control, and its expressed as Equation 2.3 Where the matrices $\mathbf{K}_a$ and $\mathbf{K}_i$ represent the stiffness characteristics of the AMB in terms of displacement and current, respectively. The variables $\mathbf{r}_a$ denote the displacements at the specific locations of

the AMB, while $\mathbf{i}_c$ correspond to the control currents applied. This controll current is static value calculated so this rotor stays on floating its normal conditions.

2.4 Rotor model

The rotor system is modeled using a combination of beam and disk elements to represent the shaft and rotating masses, respectively. Beam elements capture the shaft's flexibility and bending behavior, while disk elements account for the concentrated mass and inertia of rotating components. Couplings are included to model the connection between different rotor sections, introducing torsional stiffness and damping. AMB are integrated into the model to provide non-contact support and active control forces, which are especially important for high-speed or precision applications. (Sopanen, 2019; Sopanen, 2009)

The dynamic behavior of the system is governed by the EOM, which includes the mass matrix **M**, damping matrix **C**, stiffness matrix **K**, and gyroscopic matrix **G**. To accurately reflect real-world conditions, the EOM is extended to include additional effects such as unbalance forces, speed-dependent stiffness (centrifugal stiffening), nonlinear damping, and control forces from AMBs. These enhancements allow the model to simulate complex rotor behaviors such as resonance, whirl, and instability across a range of operating speeds. (Sopanen, 2019; Sopanen, 2009)

2.5 Damped Eigenvalue Problem

The dynamic behavior of rotating machinery is significantly influenced by its natural frequencies and mode shapes, particularly under the effects of damping and gyroscopic forces. To analyze these characteristics, the damped eigenvalue problem must be solved. This section outlines the theoretical basis and computational approach used in this thesis for determining the natural frequencies, damping ratios, and whirling modes of a rotor system using a state-space formulation. (Inman, 2014. p. 303 - 369.)

$$\mathbf{M}\ddot{\mathbf{q}} + (\Omega\mathbf{G} + \mathbf{C})\dot{\mathbf{q}} + \mathbf{K}\mathbf{q} = 0 \tag{2.4}$$

The starting point for the analysis is the homogeneous form of the damped equation of motion (Equation 2.4) where **M** is the mass matrix, **C** the damping matrix, **G** the gyroscopic matrix, and **K** the stiffness matrix. To facilitate eigenvalue analysis, this second-order differential equation is transformed into a first-order state-space system. This is achieved by defining the state variables $\mathbf{y}_1 = \mathbf{q}$ and $\mathbf{y}_2 = \dot{\mathbf{q}}$. (Chen & Gunter, 2001. p. 315 - 320.)

$$\begin{cases} \dot{\mathbf{y}}_1 = \dot{\mathbf{q}} = \mathbf{y}_2 \\ \dot{\mathbf{y}}_2 = \ddot{\mathbf{q}} = -\mathbf{M}^{-1}(\Omega\mathbf{G} + \mathbf{C})\dot{\mathbf{q}} - \mathbf{M}^{-1}\mathbf{K}\mathbf{q} \end{cases} \tag{2.5}$$

$$\dot{\mathbf{y}} = \begin{bmatrix} 0 & \mathbf{I} \\ -\mathbf{M}^{-1}\mathbf{K} & -\mathbf{M}^{-1}(\Omega\mathbf{G} + \mathbf{C}) \end{bmatrix} \begin{bmatrix} \mathbf{y}_1 \\ \mathbf{y}_2 \end{bmatrix} = \mathbf{A}\mathbf{y} \tag{2.6}$$

This Equation 2.5 order state-space form can then be written as matrix form Equation 2.6 where matrix **A** referred to system matrix of an damped case and **y** is the state vector.(Chen & Gunter, 2001. p. 315 - 320.)

In rotor dynamic analysis, free-free modes refer to the natural vibration modes of a rotor system when it is not constrained by bearings or supports. This condition is useful for identifying the inherent dynamic characteristics of the rotor itself, independent of boundary conditions.

$$\dot{\mathbf{y}} = \begin{bmatrix} 0 & \mathbf{I} \\ -\mathbf{M}^{-1}\mathbf{K}^{*} & -\mathbf{M}^{-1}\mathbf{C} \end{bmatrix} \begin{bmatrix} \mathbf{y}_1 \\ \mathbf{y}_2 \end{bmatrix} = \mathbf{A}\mathbf{y} \tag{2.7}$$

To analyze free-free modes, the shaft's angular velocity Ω is set to zero, and all bearing-related stiffness and damping terms are excluded from the system matrices. The resulting equation of motion is simplified and expressed in state-space form as Equation 2.7. On here $\mathbf{K}^*$ is the stiffness matrix without bearing.

For solution this then can be assumed to be form $\mathbf{y} = \mathbf{z}e^{\lambda t}$, where **z** vector of constants and λ is scalar value. Substituting this solution on Equation 2.6 or Equation 2.7, leading to the eigenvalue problem. (Inman, 2014. p. 320)

$$\mathbf{Az} = \lambda \mathbf{z} \tag{2.8}$$

$$\lambda_i = a_i \pm j\beta_i \tag{2.9}$$

For this problem Equation 2.8 $\mathbf{z} \neq 0$ and problem is size of $2n \times 2n$, where n is number of natural frequencies. In practice there is $2n$ eigenvalues λ_i every ith mode which appears on complex conjugate pairs form Equation 2.9. On this equation a_i is real part and can be expressed as $a_i = -\xi_i \omega_i$, j is imaginary unit and imaginary is β_i is imaginary part that can be expressed as $\beta_i = \omega_i \sqrt{1 - \xi_i^2}$. From these natural frequencies and damping ratios for each mode can be calculated. (Inman, 2014. p. 320 - 404.)

$$\omega_i = \sqrt{a_i^2 + \beta_i^2} = \sqrt{\text{Re}(\lambda_i)^2 + \text{Im}(\lambda_i)^2} \tag{2.10}$$

$$\xi_i = \frac{-a_i}{\sqrt{a_i^2 + \beta_i^2}} = \frac{-\text{Re}(\lambda_i)}{\sqrt{\text{Re}(\lambda_i)^2 + \text{Im}(\lambda_i)^2}} \tag{2.11}$$

On frequencies Equation 2.10 and damping ratios Equation 2.11 Re() and Im() denote the real and imaginary components of the complex eigenvalue λ_i respectively. This approach is applicable to both full and reduced-order models. In the case of modal reduction, the matrices used in the state-space formulation are projected onto a reduced modal basis, significantly decreasing computational cost while preserving essential dynamic characteristics.(Inman, 2014. p. 399 - 404.)

2.5.1 Whirling modes

The eigenvectors associated with the complex eigenvalues describe the mode shapes of the system. In the presence of damping, these mode shapes are complex and represent both the amplitude and phase of motion.(Chen & Gunter, 2001. p. 315 - 320.)

$$\begin{aligned}\mathbf{u}_i^*(t) &= e^{\lambda_i t}\mathbf{u}_i + e^{\overline{\lambda}_i t}\overline{\mathbf{u}}_i \\ &= 2e^{-\xi\omega_i t}[\text{Re}(\mathbf{u}_i)cos(\omega_{di}t) - \text{lm}(\mathbf{u}_i)sin(\omega_{di}t)] \\ &= 2e^{-\text{Re}(\lambda_i)t}[\text{Re}(\mathbf{u}_i)cos(\text{lm}(\lambda_i)t) - \text{lm}(\mathbf{u}_i)sin(\text{lm}(\lambda_i)t)]\end{aligned} \tag{2.12}$$

The time-dependent displacement of the ith mode can be expressed as on Equation 2.12. This expression describes an elliptical orbit in the lateral plane, characteristic of rotor whirling motion. (Chen & Gunter, 2001. p. 315 - 320.)

$$\text{sign}(\dot{\theta}) = \text{sign}(y_s z_c - y_c z_s) \tag{2.13}$$

The direction of whirl—forward or backward—is determined by the sign of the precessional rate Equation 2.13 where y_c, z_c and y_s, z_s are the real and imaginary components of the mode shape in the lateral directions. A positive sign indicates forward whirl (same direction as shaft rotation), while a negative sign indicates backward whirl. (Chen & Gunter, 2001. p. 315 - 320.)

2.5.2 Campbell Diagram

The natural frequencies of a rotor system are not constant but vary with rotational speed due to the influence of gyroscopic effects and speed-dependent stiffness and damping. To visualize this dependency, a Campbell diagram is constructed. This diagram plots the natural frequencies (typically in Hz) against the shaft rotational speed (in rpm). (Chen & Gunter, 2001, p. 59 - 61.; Genta, 2007, p. 177 - 183.)

To generate the Campbell diagram, the eigenvalue problem is solved at multiple rotational speeds. At each speed, the system matrix **A** is updated to reflect the current gyroscopic and damping conditions. The imaginary parts of the eigenvalues are then plotted to show how the natural frequencies evolve with speed. Critical speeds are identified where these

curves intersect the excitation frequency line (equal to the shaft speed), indicating potential resonance conditions. (Chen & Gunter, 2001, p. 59 - 61.; Genta, 2007, p. 177 - 183.)

2.5.3 Unbalance Response

Unbalance in a rotor system occurs when the mass distribution is not perfectly symmetric about the axis of rotation. This asymmetry generates a centrifugal force during operation, which leads to vibrations that must be analyzed to ensure safe and stable performance. (Inman, 2014, p. 160 - 161.; Lalanne & Ferraris, 1998)

$$\begin{bmatrix} F_Y \\ F_Z \end{bmatrix} = m_u r \Omega^2 \begin{bmatrix} \cos(\Omega t + \phi) \\ \sin(\Omega t + \phi) \end{bmatrix} \tag{2.14}$$

Unbalance is modeled by assigning a mass m_u at a radial distance r from the rotation axis at a specific node. The angular position of the unbalance is defined by an angle ϕ, measured from the positive Y-axis. The resulting centrifugal force components in the Y and Z directions as seen on Equation 2.14. (Lalanne & Ferraris, 1998)

$$\begin{bmatrix} F_Y \\ F_Z \end{bmatrix} = m_u r \Omega^2 \left(\begin{bmatrix} \sin(\phi) \\ \cos(\phi) \end{bmatrix} \sin(\Omega t) + \begin{bmatrix} \cos(\phi) \\ \sin(\phi) \end{bmatrix} \cos(\Omega t) \right) \tag{2.15}$$

Using trigonometric identities, this force can be expressed as a combination of sine and cosine terms as seen on Equation 2.15. This allows the unbalance force to be decomposed into two constant vectors $\mathbf{p}_s$, the sine component and $\mathbf{p}_c$,the cosine component, respectively. (Lalanne & Ferraris, 1998)

$$\mathbf{M}\ddot{q} + (\mathbf{C} + \Omega\mathbf{G})\dot{q} + \mathbf{K}q = \mathbf{F}_s \sin(\Omega t) + \mathbf{F}_c \cos(\Omega t) \tag{2.16}$$

$$q(t) = \mathbf{p}_s \sin(\Omega t) + \mathbf{p}_c \cos(\Omega t) \tag{2.17}$$

These vectors are assembled across all nodes to form global force vectors $\mathbf{F}_s$ and $\mathbf{F}_c$ as seen on Equation 2.16. The solution is assumed be in the form of Equation 2.17. (Lalanne & Ferraris, 1998)

$$\begin{bmatrix} \mathbf{K} - \Omega^2\mathbf{M} & \Omega(\mathbf{C} + \Omega\mathbf{G}) \\ -\Omega(\mathbf{C} + \Omega\mathbf{G}) & \mathbf{K} - \Omega^2\mathbf{M} \end{bmatrix} \begin{bmatrix} \mathbf{p}_s \\ \mathbf{p}_c \end{bmatrix} = \begin{bmatrix} \mathbf{F}_s \\ \mathbf{F}_c \end{bmatrix} \tag{2.18}$$

Substituting this into the equation of motion and collecting terms leads to a linear system of Equation 2.18. Solving this system for a given rotational speed Ω yields the steady-state response of the rotor due to unbalance. The resulting displacement vector $q(t)$ describes the orbit of the rotor centerline, which is critical for evaluating vibration levels and ensuring reliable operation. (Lalanne & Ferraris, 1998)

3 Case Study

Four different cases are studied and compared to reference case. These cases have similar components but different layouts and all these are explained on this chapter.

Table 1 presents the rotor configurations considered in this study. Case R represents the reference design, while the other configurations are numbered from 1 to 4. These numbered cases are compared both to the reference case and to each other to evaluate differences in rotor dynamics and design characteristics. All cases contains generator (Gen) and numbered cases contains coupling (Coup) other components and their abbreviations on table are as follows:

- High Pressure Turbine (HPT) as High Pressure Turbine
- High Pressure Compressor (HPC) as High Pressure Compressor and numbers indicates order of flow direction
- RAMB as Radial Active Magnetic Bearing and numbers are order from left to right
- AAMB as Axial Active Magnetic Bearing and numbers are order from left to right

Table 1: Case assembly layouts

Case	**Rotor assembly**									
Case R	HPT	RAMB 1	Gen	RAMB 2	AAMB	HPC2	HPC1			
Case 1	HPT	RAMB 1	Gen	RAMB 2	AAMB 1	Coup	HPC2	RAMB 3	AAMB 2	HPC1
Case 2	HPC1	HPC2	RAMB 1	Gen	RAMB 2	AAMB 1	Coup	AAMB 2	RAMB 3	HPT
Case 3	HPT	RAMB 1	Gen	RAMB 2	AAMB 1	Coup	RAMB 3	AAMB 2	HPC2	HPC1
Case 4	RAMB 1	Gen	RAMB 2	AAMB 1	Coup	HPT	RAMB 3	AAMB 2	HPC2	HPC1

Each of the HPT and HPC 1 and 2 carries its own clearance envelope. When these components are repositioned, their clearance boxes move with them, which can slightly change the overall assembly length. While main clearances remain consistent, this approach simplifies the study, even though it affects analyses since the cases are not optimized.

3.1 Possible cases

These four numbered cases are first analyzed which are good for next steps related to possible assembly, weight distribution and heat transfer. First showing reference case and related to that numbered cases cases are compared, component order gone through as seen also Table 1, showing image on case, listing evaluation of assembly, weight, cooling and heath expansion. These concerns should be studied after rotor dynamic study is concluded.

3.1.1 Case R

On reference case, called as Case R, active part shaft contains all AMBs on order radial, radial, axial. Components around rotor are listed left to right as turbine, generator, compressor 2, compressor 1 as can seen on Figure 11 .

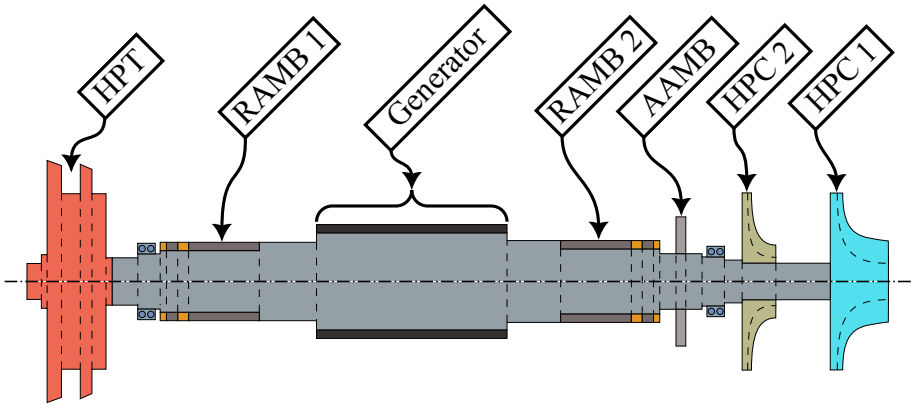

Figure 11: Case R layout

3.1.2 Case 1

On Case 1 active part is same as reference case but rotor is extended using coupling and there is another AAMB and RAMB pair. Components around rotor are listed left to right as turbine, generator, coupling, compressor 2, extension shaft AMBs, compressor 1 as can seen on Figure 12.

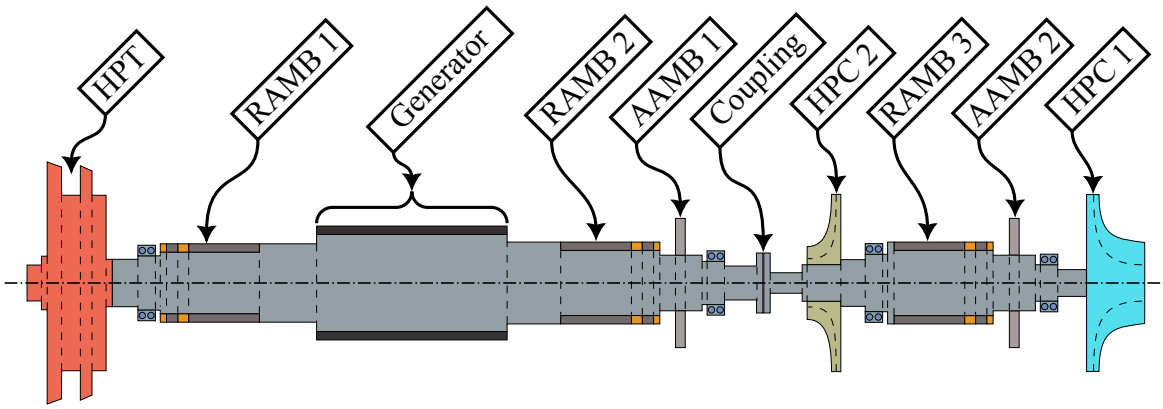

Figure 12: Case 1 layout

3.1.3 Case 2

On Case 2 active part is same as reference case but rotor is extended using coupling and there is another AAMB and RAMB pair. Components around rotor are listed left to right as compressor 1, compressor 2, generator, coupling, extension shaft AMBs, turbine, as can seen on Figure 13.

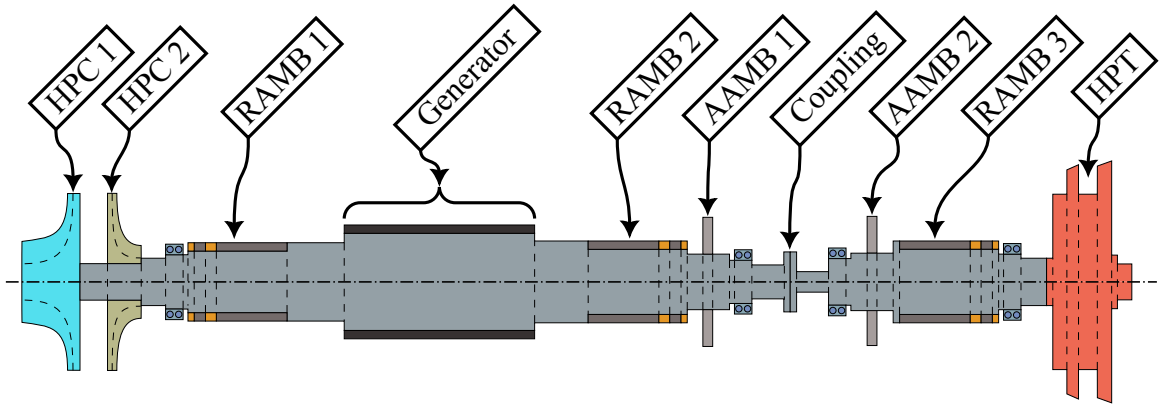

Figure 13: Case 2 layout

3.1.4 Case 3

On Case 3 active part is same as reference case but rotor is extended using coupling and there is another AAMB and RAMB pair. Components around rotor are listed left to right as

turbine, generator, coupling, extension shaft AMBs, compressor 2, compressor 1 as can seen on Figure 14.

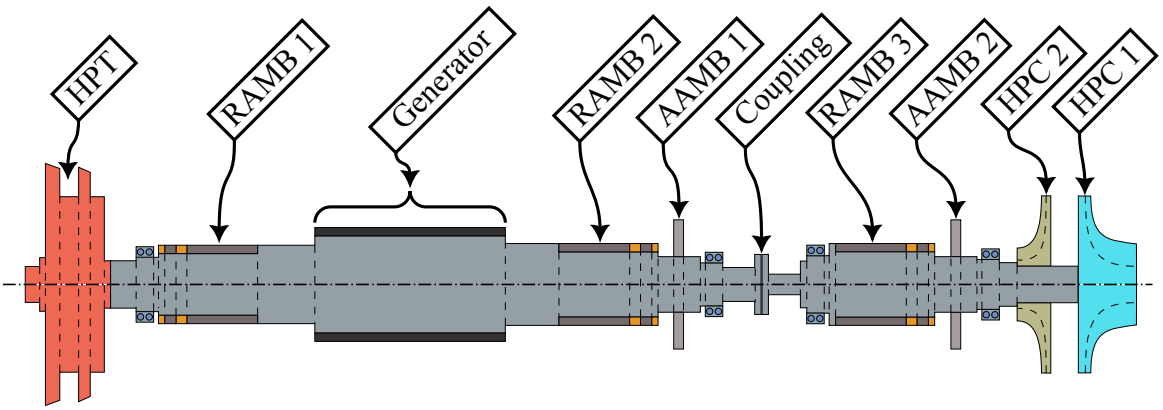

Figure 14: Case 3 layout

3.1.5 Case 4

On Case 4 active part contains only two RAMBs but rotor is also extended using coupling and there is another AAMB and RAMB pair. Components around rotor are listed left to right as generator, coupling, turbine, extension shaft AMBs, compressor 2, compressor 1 as can seen on Figure 15.

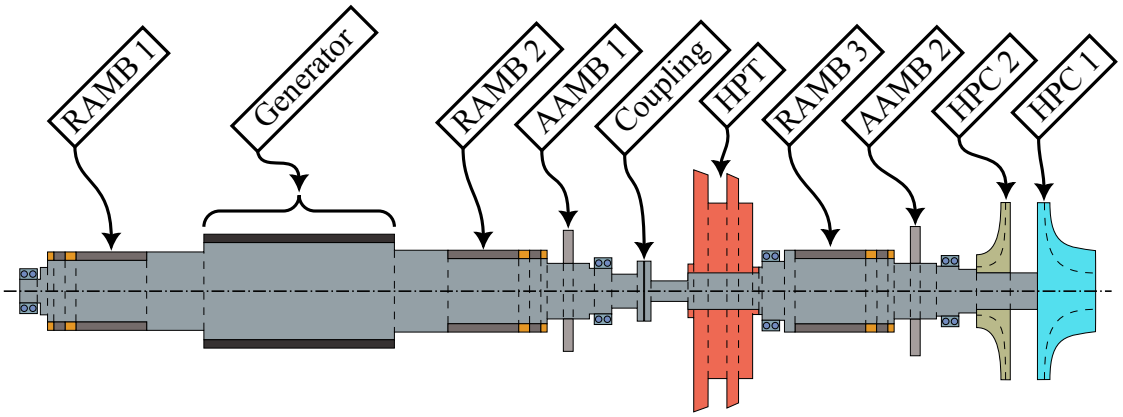

Figure 15: Case 4 layout

3.2 Model properties

Choudhury et al. (2025) developed an initial design using a multidisciplinary approach for high-speed electrical machines, and this thesis uses one of those designs as a reference case. This provides a starting point for comparing the cases with each other and with the reference configuration, allowing analysis of how these designs behave differently. In these cases, some parameters remain the same, as shown in Table 2 and Table 3, which include process cycle parameters and turbomachine components.

Table 2: Inputs for the process cycle

Process parameters	**Value**	**Unit**
Power (Electrical)	2.70	MW
Under Speed	12 000	rpm
Nominal Speed	15 000	rpm
Over-speed	18 000	rpm

Table 3: Turbomachinery components

	Values for components			
Parameters	**HPC 1**	**HPC 2**	**HPT**	**Unit**
Axial length	148.00	85.00	188.00	mm
Outlet diameter	469.68	473.40	-	mm
Hub diameter	22.00	80.00	-	mm
Mean diameter	-	-	583.70	mm
Mass (kg)	18.26	15.25	108.16	mm
Polar moment of Inertia	0.30	0.31	4.60	kg·m^2
Diametral moment of Inertia	0.18	0.16	2.30	kg·m^2

On 3-RAMB cases coupling is same on all designs. Coupling is modeled as spring which values can be seen on Table 4.

Table 4: Coupling parameters

Stifness Parameters	**Value**
Axial	$38.7 \cdot 10^6$
Radial	$317 \cdot 10^6$
Torsoinal	$2.80 \cdot 10^6$
Bending	$0.121 \cdot 10^6$

Rotor main shaft and extension shaft length changes slightly between cases and these differences are listed on Table 5, total weight is also affected on this changing length. These

lengths and weights take account only shafts and what are connected to those as can be seen on different cases as an example Case R. All 3-RAMB cases are close to each other on length and weight, Case 4 lengths and weight is outlier on these case being longest and heaviest.

Table 5: Case shaft lengths and total weight.

Case	**Main Shaft** [mm]	**Extension Shaft** [mm]	**Coupling length** [mm]	**Total length** [mm]	**Total weight** [kg]
Case R	2044	-	-	2044	601
Case 1	1657	802	166	2625	673
Case 2	1712	679	166	2557	669
Case 3	1657	734	166	2557	669
Case 4	1469	1110	166	2745	687

AMB have stiffness and damping on them, these values are presented on Table 6.

Table 6: Active magnetic bearing stiffness and damping

Case	**RAMB**		**AAMB**	
	stiffness	**damping**	**stiffnes**	**damping**
Case R	$27 \cdot 10^6$	$47 \cdot 10^3$	$38 \cdot 10^6$	$47 \cdot 10^3$
Case 1	$18 \cdot 10^6$	$53 \cdot 10^3$	$38 \cdot 10^6$	$53 \cdot 10^3$
Case 2	$18 \cdot 10^6$	$53 \cdot 10^3$	$38 \cdot 10^6$	$53 \cdot 10^3$
Case 3	$18 \cdot 10^6$	$53 \cdot 10^3$	$38 \cdot 10^6$	$53 \cdot 10^3$
Case 4	$18 \cdot 10^6$	$54 \cdot 10^3$	$38 \cdot 10^6$	$54 \cdot 10^3$

As these shafts are slightly different from each other unbalances are also different as trying to find most serious case. These differences are shown on Table 7, making the system more manageable places where unbalances are added are predetermined, these being HPT, generator center, HPC 1 & 2. On this table is provided unbalance from center of shaft and angle.

Table 7: Unbalance values on cases Case R, Case 1 and Case 4

Case	**HPT**		**Generator**		**HPC 1**		**HPC 2**	
	g · mm	[rad]	g · mm	[rad]	g · mm	[rad]	g · mm	[rad]
Case R	764	0	957	$\pi/2$	230	0	230	$\pi + \pi/2$
Case 1	764	0	1071	π	230	$\pi + \pi/2$	230	0
Case 2	764	0	1071	$\pi/2$	230	$\pi + \pi/2$	230	$\pi + \pi/2$
Case 3	764	0	1071	π	230	$\pi + \pi/2$	230	$\pi + \pi/2$
Case 4	764	0	1094	π	230	π	230	π

3.3 Matlab toolbox used on study

Rotor Bearing Dynamics (RoBeDyn) is a MATLAB-based computational toolbox designed for the dynamic analysis of rotor-bearing systems. It provides a comprehensive set of tools for modeling, simulating, and visualizing the behavior of rotating machinery under various operating conditions. The toolbox is built on the finite element method and supports the use of beam elements, mass elements, spring-damper systems, and both ball and journal bearings. (Sopanen, 2019; Sopanen, 2009)

RoBeDyn enables users to perform a wide range of analyses, including the calculation of free-free vibration modes, Campbell diagrams, unbalance responses, and threshold speeds for dynamic instability. It also includes routines for computing bearing stiffness and damping coefficients, which can vary with speed and load. The toolbox supports both full and reduced-order modeling and includes visualization tools for mode shapes and rotor deformation. Its open structure allows for customization and extension, making it suitable for both research and educational purposes in rotor dynamics.(Sopanen, 2019; Sopanen, 2009)

Kurvinen et al. (2021) expanded this toolbox to make the design process more user-friendly. This updated toolbox supports a design space method for conceptual design of high-speed electric machines, integrating analytical models and rotordynamics to define baseline dimensions from application requirements. These dimensions serve as variables for design space exploration and sensitivity analysis, enabling rapid iterations and optimization while providing a foundation for detailed design.

4 Results and Comparative Analysis of Rotor Layouts

This section presents a comparative evaluation of multiple rotor layouts to identify the most suitable candidates for a detailed rotordynamic analysis. This section outlines the process of systematically eliminating less favorable designs based on key performance criteria such as assembly, ease of implementation, natural frequency range, and critical speed. The goal is to retain only those designs that demonstrated stable dynamic behavior and met operational requirements, ensuring a focused and efficient analysis in the subsequent sections.

4.1 Shortlisting number of cases based on mechanical complexity and initial dynamic analysis

In this section, each case is evaluated based on ease of assembly, weight distribution, cooling, thermal expansion, and initial rotordynamic analysis. Based on this evaluation, the number of cases are shortlisted for further analysis.

In Case 1, the weight distribution on the shaft is well balanced as the compressors are significantly lighter that the turbine, HPC 1 and 2 are attached on either side of the 3rd RAMB. From assembly point of view, this design brings forward some complexities, especially since the HPC 2 has to be shrink fitted to the shaft after other components are installed on the extension shaft. On main shaft turbine heat can be managed. In the extension shaft where HPCs being added to both side of 3rd RAMB, this exposes both ends to thermal challenges that increases heat.

In Case 2, the large overhang due to the HPT can be difficult for the extension shaft to accommodate and the design would require larger clearances. Furthermore, the turbine would generate significant amount of heat. As the shaft cannot be extended axially the high temperature from the turbine can affect the safety bearings and the 3rd RAMB material properties, even with the use of shielding structure.

In Case 3, the weight distribution on the extensions shaft is unbalanced as the compressors are installed to end, however on whole rotor its more balanced as turbine is at other end. From assembly point of view, this design brings forward some complexities, especially since the HPC 2 has to be shrink fitted to the extension shaft. Heat can be managed here by simply using shielding structure.

In Case 4, the main shaft offers excellent weight balance, as there is no extra components on it. However, on extension shaft there is HPT and HPC 1 and 2, making this relatively heavy. As turbine is on coupling side provides this some support. As on also Case R and Case 1, HPC 1 and 2 are installed to end, which makes slight overhang. Assembly is challenging as turbine is connected to coupling side and HPC 2 has to be shrink fitted to the shaft. This assembly layout can need heavy modifications due heating, as making clearances larger thus effecting heavily rotordynamic evaluation.

Table 8 shows the rating of each case when evaluated based on these parameters. From the analysis of the mechanical design complexity and assembly procedure, the Case 1 and Case 4 are more complex than the others because of the integration of one of the process stages in between the generator and the extension shaft. It should be noted that Case 4 provides the possibility of creating a stand alone extension shaft design with all stages, that can be combined with any standard commercially available electric machine. However, the heat from the turbine and the associated combustion chamber which can be assumed to be located in the vicinity as well, should be carefully considered in the design calculations and dealt with adequate cooling. Furthermore, this layout has better controllability for the axial thermal expansion of the shaft with the turbine located in between the two AAMBs and additional room for thermal expansion for the coupling. On the other hand, the layout in Case 2 might be difficult to implement feasibly because of the large overhung from the turbine at the end of the extension shaft. Overall, from mechanical design and layout point of view, case 1 and 3 seem more feasible but none of the cases can be eliminated just yet based on the design constraints alone.

Table 8: Case difficulty matrix

	Case R	Case 1	Case 2	Case 3	Case 4
Assembly	● ● ● ● ●	● ● ● ●	● ● ●	● ● ● ● ●	● ● ●
Weight Motor Shaft	● ● ●	● ● ●	● ● ● ●	● ● ●	● ● ● ● ●
Weight Extension Shaft	-	● ● ● ● ●	●	● ● ● ●	● ●
Cooling	● ● ● ● ●	● ● ● ●	●	● ● ● ● ●	●
Thermal expansion	● ● ● ● ●	● ● ●	● ●	● ● ●	● ● ●

When designing the rotor one consideration is weight, length of assembly. There is no length, or weight restrictions on this study. However, in practical applications, these are still often restricted due available installation space, being it either on larger hall or an moving vessel.

From Table 5 total length and weigh differences can be calculated, numbered cases are compared to Case R. As shown on Table 9, Case 2 and Case 3 are shorter and weight less, this difference is on length can be deciding factor on certain installations. These variations on length and weight represents cumulative differences when considering the entire machine. This reason its important to check even on this study the difference on these cases, usually this is done as constraints and defined before the design process, as these influence design decisions.

Table 9: Length and weight differences related to Case R

Case	Lenght	Weight
Case 1	28.42 %	11.98 %
Case 2	25.10 %	11.13 %
Case 3	25.10 %	11.13 %
Case 4	34.30 %	14.31 %

To shortlist the cases for the next steps, initial rotortordynamic calculations are carried out. Table 10 shows the critical speed for the first few bending modes for all numbered cases (layouts with extension shaft) along with the benchmark case, Case R. The desired operational speed is 15000 rpm and safety range is 12000 - 18000 rpm. From that perspective, all cases have the second backward whirling (BW) bending mode within the safety range of operation. However, since BW do not result in resonance and can be taken into account in the control design, at this stage the focus is on the first forward whirling (FW) critical speeds. For Case 2, the first FW critical speed is very close to the operational speeds. Due to the possibility of

high vibration, Case 2 is eliminated at this stage. Case 1, Case 3 and Case 4 display better dynamic properties. However, Case 1 and Case 3 are similar in terms of layout and dynamics, with Case 3 having critical speeds slightly closer to the operational range. Therefore, for the sake of conciseness, out of these two, only Case 1 is considered for detailed rotordynamic analysis, other case considered is Case 4 as it shows initially promising rotordynamic results, even if layout and assembly are less favorable.

Table 10: Cases initial critical speeds analysis as operational speed is 15000 rpm.

Case	**Bending mode Critical Speeds** [rpm]				
	1st. BW	**1st. FW**	**2nd. BW**	**2nd. FW**	**3rd. BW**
Case R	7773	9649	12419	19939	19456
Case 1	9271	12559	14190	20832	22417
Case 2	10076	13941	16092	22244	23245
Case 3	9344	12952	14739	21768	23054
Case 4	9098	9744	15570	>25000	>25000

4.2 Unsupported (Free-free) vibration modes

To visualize the rotor behavior without support, free-free mode plots were generated (Figures 16 and 17a to 17c), from these can be seen how rotor and extension shaft behaves, from these plots also Table 11 is made to easily compare the natural frequencies in each case.

On Table 11 can be seen frequency pairs and torsion and axial modes, which are marked with ”T/A”. As the rotordynamic analysis begins here, these results are used later in this chapter. On Figure 16 are shown rigid modes of each case, while Figures 16b and 16c illustrates also V-shape mode which is bending mode even if both shafts are not bending, reasoning being coupling is bending. These modes are compared to Campbell diagram modes at zero rpm, from this can be found how much bearing support affects system mode shape frequencies.

Case R have two rigid modes that are slightly different as on first turbine is moving more and compressor end stays closer to nodal location. On second rigid mode turbines higher weight resists displacement and compressor end displaces more. On Figure 16b and Figure 16b

Table 11: Natural frequencies of modes on Case R, Case 1 and Case 4 when near zero frequencies has been filterer out.

Case	Natural Frequensies [Hz]							
Case R	144.5	144.5	257.7	257.7	258.0 T/A	410.6	410.6	434.8 T/A
Case 1	9.5	9.5	99.9 T/A	119.2 T/A	183.3	183.3	281.9	281.9
Case 4	8.5	8.5	85.1 T/A	95.0 T/A	155.1	155.1	345.7	345.7

more interesting mode is this V-shaped mode, along with the components influencing this shape. Figure 16b turbine overhang keeps mode end close to nodal location at its end, as this coupling bends. At Figure 16c turbine being between generator and extension shaft near coupling affects negatively on bending as its close to coupling affecting it more easily, thus coupling is bending more than on Case 1 and on lower frequency by small difference.

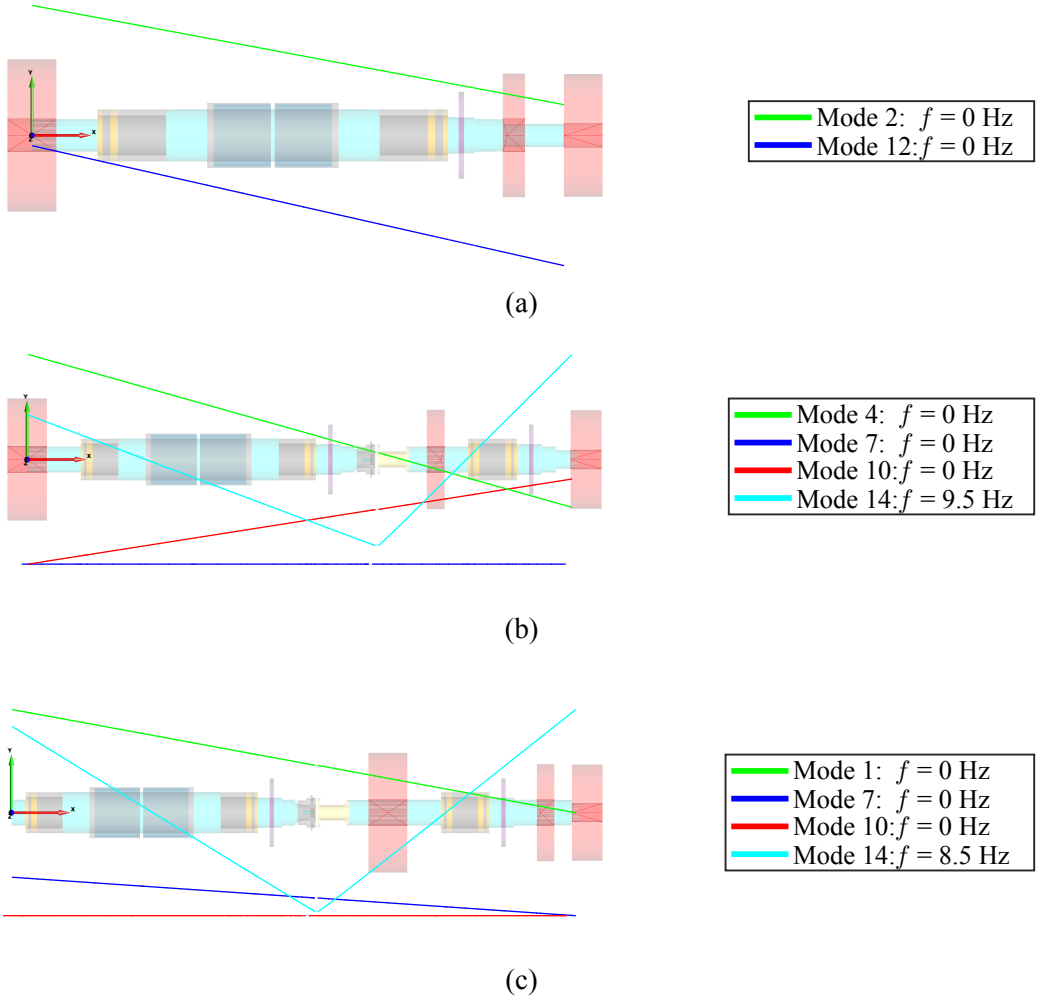

Figure 16: Near zero frequency Free-Free diagrams from (a) Case R, (b) Case 1, (c) Case 4

Figure 17 shows the first bending modes where the shaft is bending from Case R, Case 1, and Case 4. Figures 16 and 17 was checked to determine where bending is affecting and which shafts (main shaft and extension shaft) are involved; these can be seen at Table 12 (Case R is added here as a reference). As can be seen, the first bending mode in the numbered cases does not exhibit bending at either shaft; this is due to the couplings lower stiffness. In the second mode, both shafts are bending, though the bending of the couplings is not prominently visible. In the third mode, Case 1 shows that the main shaft bends twice and the extension shaft only once; the coupling might be bending here with the shafts. Case 4 In the third mode, these bends occur in the opposite order: the main shaft bends once and the extension bends twice, and the coupling is bending with the shafts. In the fourth mode, these bendings remain the same across cases, but there is bending over the coupling. These modes are needed to confirm if the modes are excited, how the supports affect mode shapes and frequency.

Table 12: Higher frequency bendings on main and extension shaft on cases Case R, Case 1 and Case 4. Main is shaft where generator is and Ext is extension shaft

	1st.		**2nd.**		**3rd.**		**4th.**	
Case	**Main**	**Ext**	**Main**	**Ext**	**Main**	**Ext**	**Main**	**Ext**
Case R	1	-	2	-	3	-	4	-
Case 1	-	-	1	1	2	1	2	1
Case 4	-	-	1	1	1	2	1	2

On Figure 17a free-free bending modes turbine shaft is relatively short before diameter increases on next part (RAMB section of shaft), this affects the amplitude on turbine end. Other hand compressor amplitude is larger even as there is less weight, reasoning here is longer and thinner shaft. This distance provides leverage from AMB to HPC 1, this smaller diameter decreases stiffness which then bends rotor easier. Figure 17a first bending mode crosses x-axis near RAMB sensor and might make some issues on start up or run time. Second and third modes observability is better as plotted line is not crossing nodal location near RAMB sensor node.

Figure 17b represents Case 1 unsupported vibration bending modes have same turbine layout as Case R, amplitude of this first section is also smaller. As external shaft HPCs are both side of RAMB balancing this shaft, keeping amplitude this compressor end smaller. On second

bending mode, plot line crosses x-axis near RAMB sensor, could be challenge to observe displacement. Other two RAMB sensors locations there is no x-axis crossing either of modes. As mentioned earlier main shaft bends two times, this is related to turbine being on main shaft this extra weight and inertia, keeps this end at place and shaft needs to bend. On extension shaft as there is more balanced layout haves only one bend. Near coupling there is most amplitude, this is because couplings lower stiffness and parts where its connected are smaller diameter.

Case 4 unsupported vibration bending modes are shown Figure 17c, on here main shaft have only few components and these components does not add lot weight. Also this shaft is has larger diameter compared to extension shaft and extension shaft being almost as same length as main shaft affects mode shapes this layout. All components which contribute to weight being on extension shaft makes it bend more than main shaft. Turbine being between RAMBs near coupling have some support from coupling, but as this is smaller diameter shaft, stiffness is lower and thus bends shaft easier. For this reason extension shaft is bending twice and main shaft only once. Second bending mode amplitude is largest at compressor end, there is same problem as at Case R longer and smaller diameter of the shaft with weight at the end. Third mode highest amplitude is near coupling, turbine here is exciting more. On fourth mode there is bending over coupling and main shaft bending once, for this reason coupling main shaft side is highest amplitude. Observability of these modes seems to be good as all on all modes as plot is not crossing x-axis more than once near RAMBs sensor location.

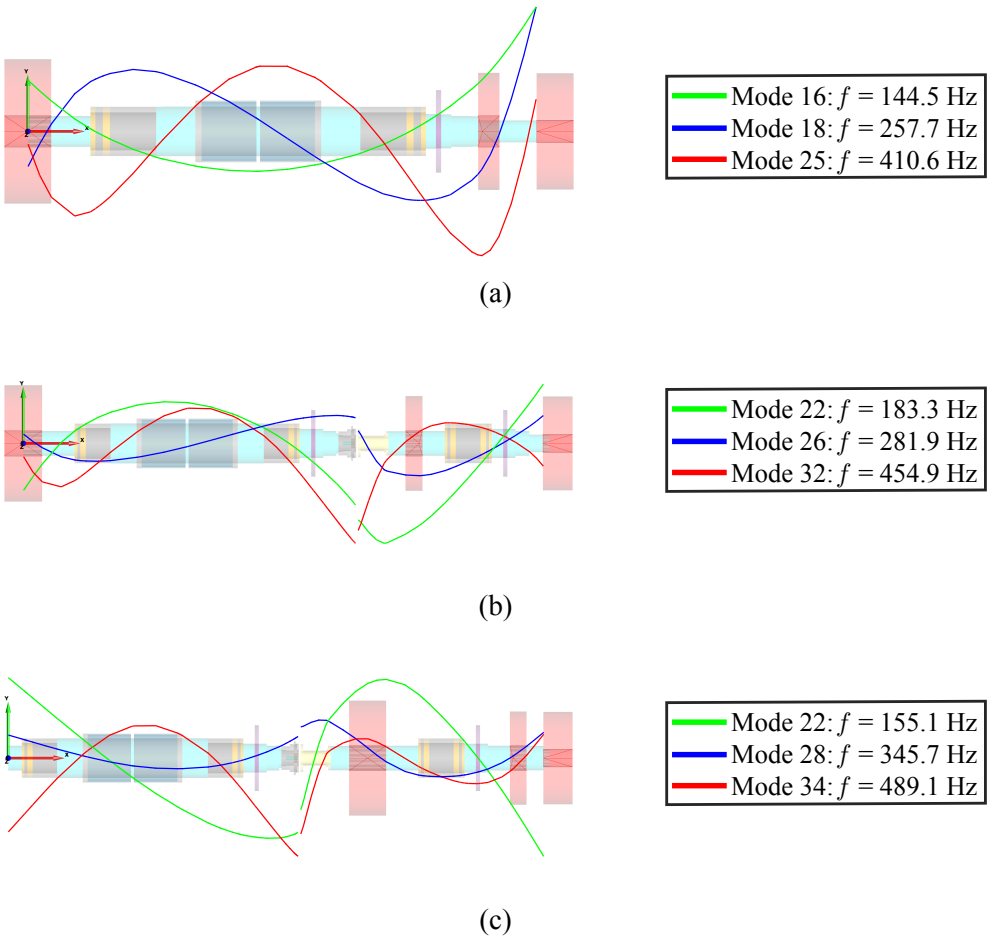

Figure 17: Bending Free-free modes of (a) Case R, (b) Case 1 and (c) Case 4.

4.3 Detailed case analysis

On this section all cases are gone through more detailed as, Figures 18, 21 and 24 shows the Campbell diagrams, Figures 19, 22 and 25 shows the unbalance response, and Figures 20, 23 and 26 shows the mode shape plot for the supported rotor for the modes resulting in the resonance peaks in the unbalance response.

The zero speed natural frequency in the Campbell diagrams after 50 Hz, show 0.5 - 2 % relative increase compared to free-free natural frequencies. This change is due to the properties of AMB, however it is not significant as AMB stiffness are relatively low. Before 50 Hz line these modes are supported by AMBs and thus this increase on frequency on modes. The Campbell diagrams (Figures 18, 21 and 24) shows the first 10 to 15

mode-shapes and their variation with speed. This also includes the torsional modes for a more comprehensive analysis.

To reach the operational speed on Case R, Case 1 and Case R, several modes should be crossed in operation. First, the rigid modes need to be crossed (between $20 - 50$ Hz). However, those are crossed at relatively lower speed (under 5000 rpm) and do not generate significant vibration as can be seen from the unbalance plots (Figures 19, 22 and 25).

4.3.1 Reference case analysis

On Case R the first FW bending mode is more critical, as even with the permissible unbalance (Table 7), the first FW shows significantly large amplitude in the HPC 1 location in Figure 19. As can be seen from Figure 20a the HPC 1 has relatively larger modal displacement due to the overhung disc and thinner end shaft as mentioned at Figure 17a. More damping is needed to cross the first FW mode, should be supplied by the AMB.

RAMB sensor amplitude seems to be low (on Figure 19), might be an issue as the mode might be difficult to observe from the sensor locations in this layout, this can be also seen at Figure 20a. In the safety region of operation, however, the lateral vibration remains low. There are two modes in the safety range at Figure 18, however the ninth mode (first critical speed inside of safety margin) is a BW mode which is not excited because the bearings are isometric. The tenth mode is a torsional mode which can be irrelevant depending on the applied frequency of the generated and external torques.

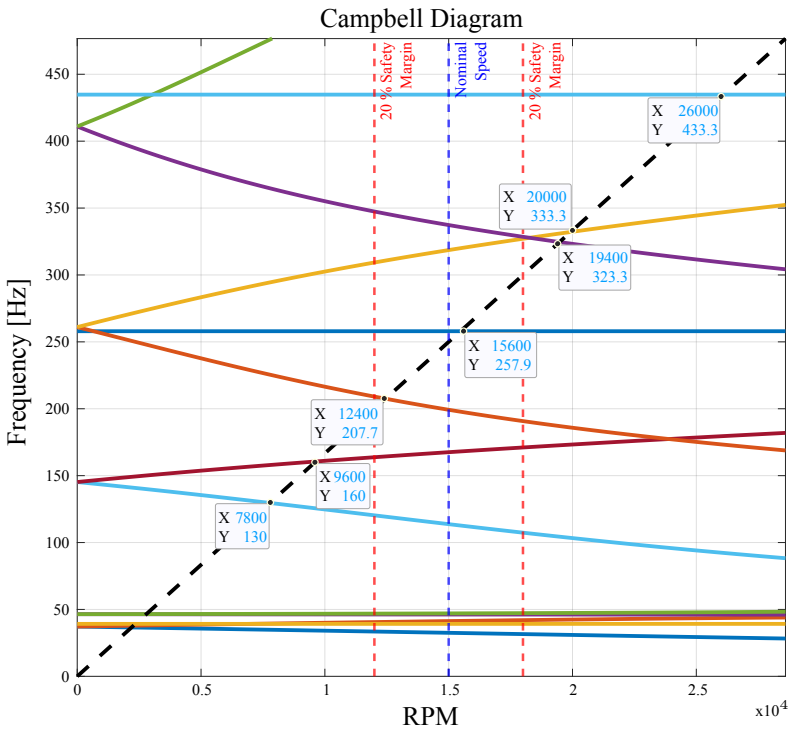

Figure 18: Campbell diagram of Case R showing critical speeds, safety margin range and operational speed

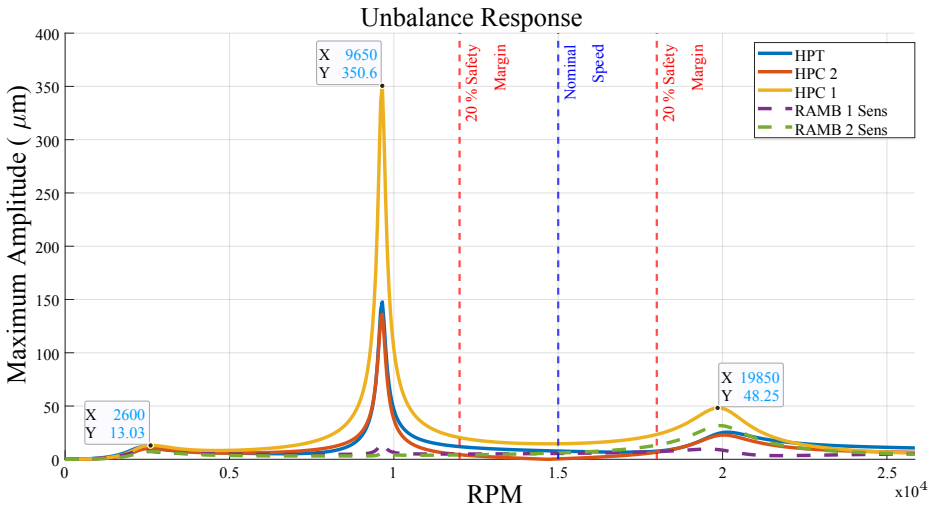

Figure 19: Case R unbalance response of different nodal locations, these being High Pressure Turbine, High Pressure Compressors, RAMB sensors locations.

After safety margin there is also one peak and this mode is second FW mode Figure 20b, this resembles also free free mode, and as this is further from safety margin area, also its

observability is higher than first mode. On Figure 20c is shown mode shape on operational speed and largest amplitude there is at HPC 1, other RAMB sensor location crosses x-axis near. This can be challenge but other RAMB is almost at bend peak and this helps observe displacement.

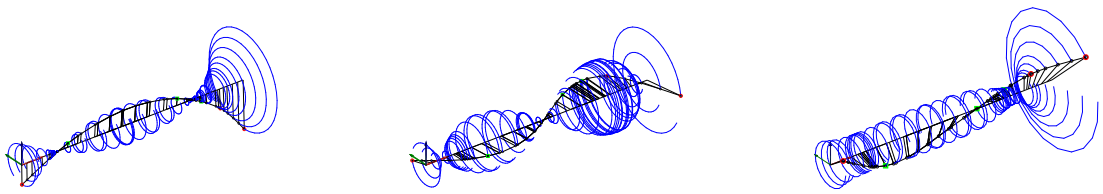

(a) (b) (c)

Figure 20: Whirling mode shapes of Case R at 15000 rpm, (a) is first FW bending modes at 168 Hz, (b) is second FW bending mode at 319 Hz and (c) Operational mode shape at 15000 rpm with maximum amplitude of 18.5 μm.

4.3.2 Case 1 analysis

From Figure 21 can be seen that after 50 Hz there are two torsional modes, which are needed to cross when the machine is warming up and accelerating to operational speed, these torsional modes which can be irrelevant depending on the applied frequency of the generated and external torques. On Case 1 the second FW bending mode is more critical, as even with the permissible unbalance (Table 7), the second FW shows large amplitude in the HPC 2 location in Figure 22. Amplitude is one third of Case R highest peak, reason for this smaller peak is HPC 2 is between two RAMBs. On other hand this coupling and smaller diameter allows this movement more easily due lower stiffness.

From Figure 23a be seen the HPC 2 has relatively larger modal displacement. As this mode is smaller and also inside of operational safety range, depending on how effectively and reliable RAMB can apply damping, this could be used in this layout. RAMB sensor displacement seems to be smaller side same as on Case R. Other critical speed on safety range is third BW bending mode which is not excited because the bearings are isometric, this mode is also before operational speed. On operational speed Figure 22 lateral vibration remains slightly higher than on Figure 19 and on over speed it lower.

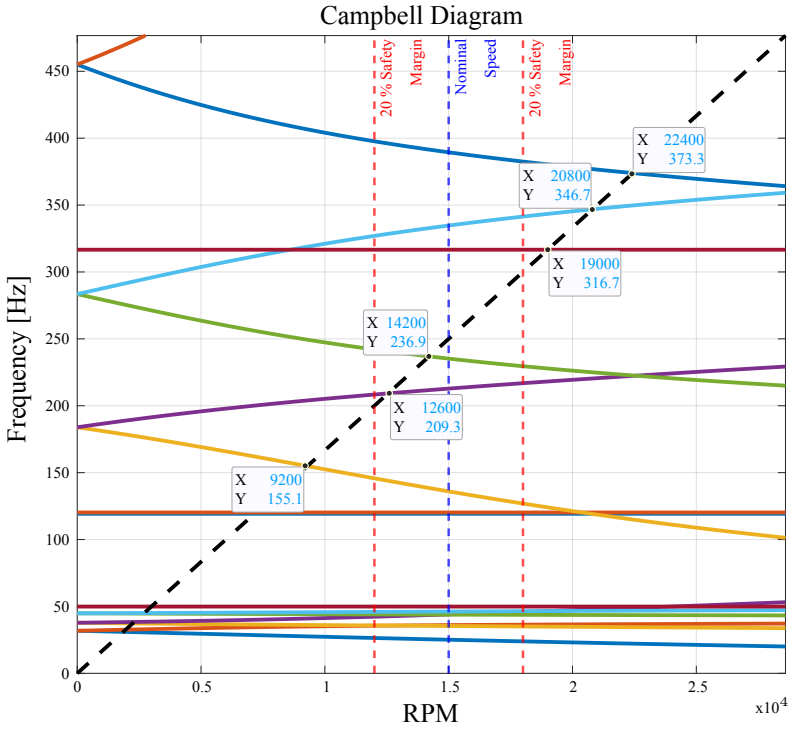

Figure 21: Campbell diagram of Case 1 showing critical speeds, safety margin range and operational speed.

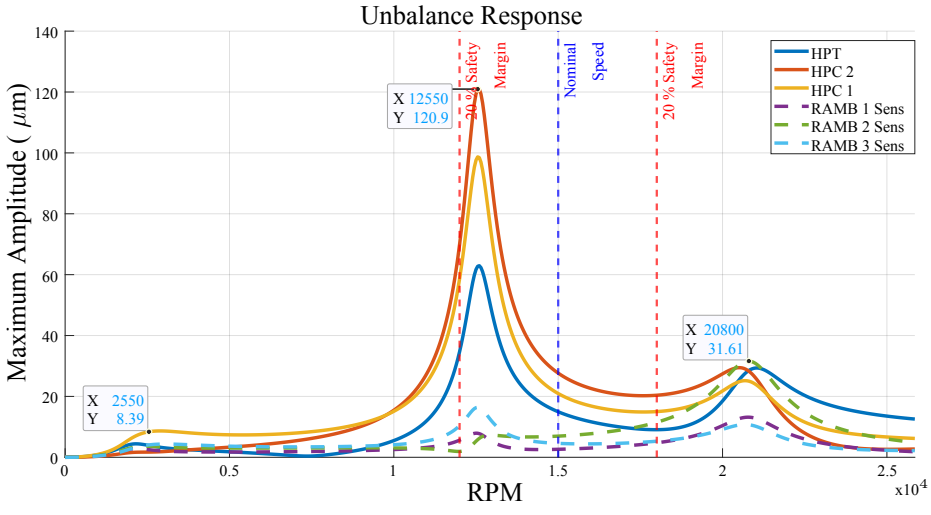

Figure 22: Case 1 unbalance response of different nodal locations, these being high pressure turbine, high pressure compressors and RAMB sensors locations.

After over speed there is also peak and this mode can be seen at Figure 23b, this mode highest amplitude seems to bee at coupling. Observability is good as, RAMBs sensors are

not crossing x-axis. Figure 23c shows mode shape on operational speed, on this mode there is highest amplitude before HPC 2, near coupling section. There is some concerns as RAMB sensors are crossing x-axis and thus observability could be challenging.

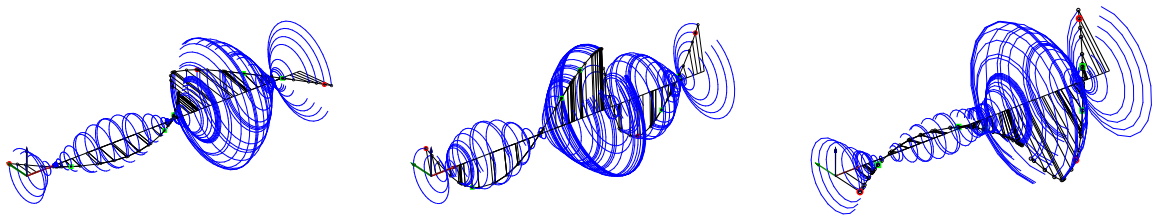

(a) (b) (c)

Figure 23: Whirling mode shapes of Case 1 at 15000 rpm, (a) at 213 Hz is second FW bending mode, (b) at 335 Hz is third FW bending mode and (c) Operational mode shape at 15000 rpm with maximum amplitude of 18.6 μm.

4.3.3 Case 4 analysis

Figure 24 after 50 Hz there is two torsional modes that are needed cross when machine is warming up and climbing to operational speed, these mode which can be irrelevant depending on the applied frequency of the generated and external torques. On Case 4 unbalance response of different nodal locations, these being high pressure turbine, high pressure compressors, radial AMB sensor locations the amplitude of highest peak is low being less than tenth of Case R highest peak. On this layout turbine is between RAMBs, these provide it support to staying on place. Even as this is lower amplitude observability here stays on same range as on Case R and Case 1.

Second FW bending mode low amplitude makes is not as critical, as RAMBs applying effective damping force should be easier. largest amplitude on this second FW is at HPC 1 which is on compressor end and this as mentioned on Figure 17c is due overhung and smaller diameter on shaft. As this peak being outside of safety range should not be a challenge. There is only one critical speed at safety range, this being third BW bending mode and is not excited because the bearings are isometric, this mode is close to operational speed.

Next peak on Case 4 unbalance response of different nodal locations, these being high pressure turbine, high pressure compressors, radial AMB sensor locations is out of figure and thus is not on safety range on any case. From Figure 26b can be found that third FW bending mode frequency is higher than any other modes until now and from Figure 24 can be seen that this modes critical speed is upper corner of diagram being close to 30000 rpm. Operational speed mode is seen at Figure 26c, this mode amplitude is 13.2 μm, this highest amplitude is at generator non driven end, observability on this mode is lower side also and could be challenging.

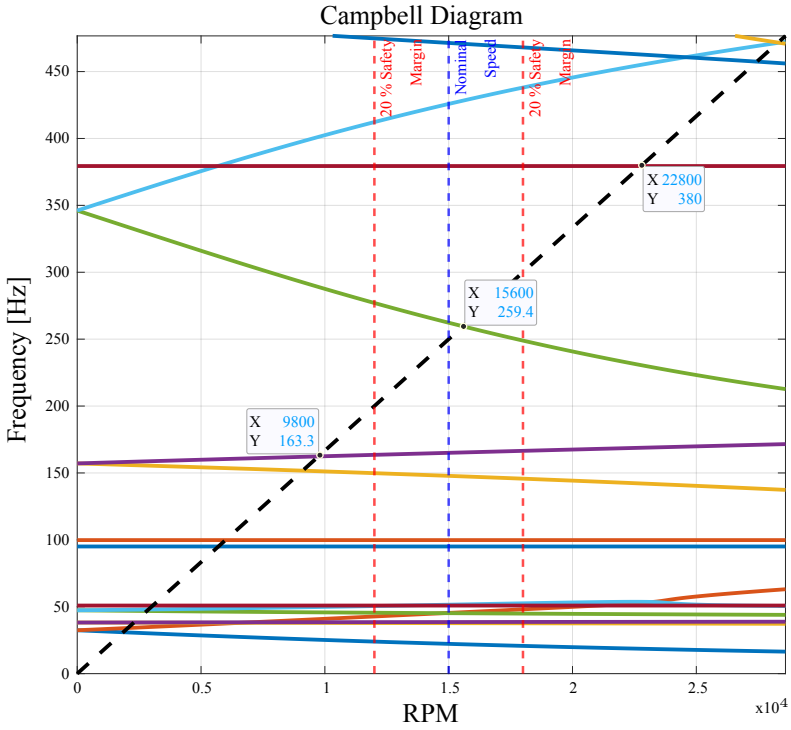

Figure 24: Campbell diagram of Case 4 showing critical speeds, safety margin range and operational speed

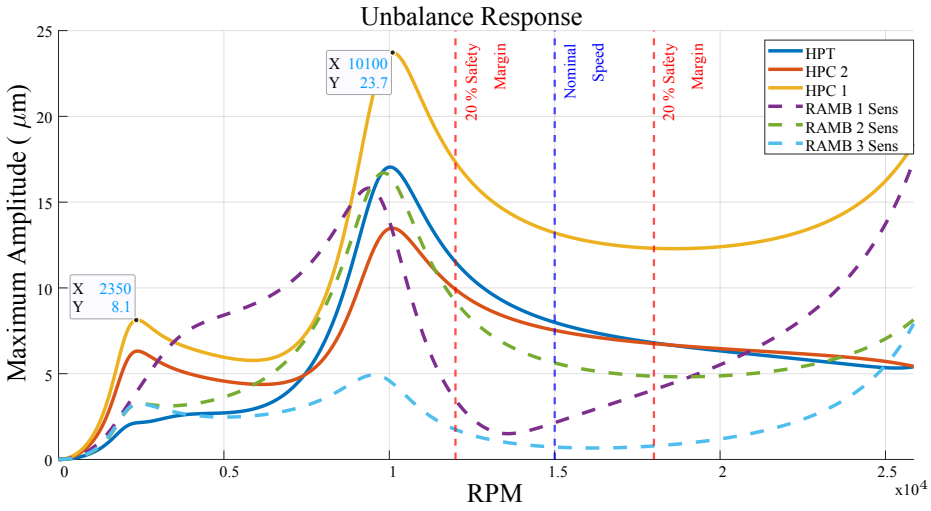

Figure 25: Case 4 unbalance response of different nodal locations, these being high pressure turbine, high pressure compressors, radial AMB sensor locations.

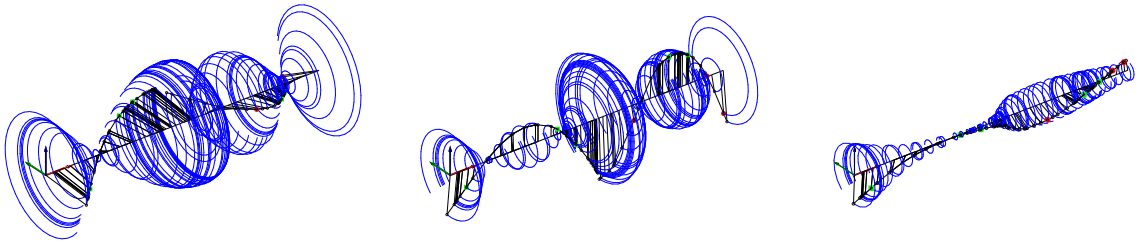

(a) (b) (c)

Figure 26: Whirling mode shapes of Case 4 at 15000 rpm, (a) at 165.0 Hz is second FW bending mode, (b) at 425.8 Hz is third FW bending mode and (c) Operational mode shape at 15000 rpm with maximum amplitude of 13.2 μm.

5 Conclusions

This study focused on the design and dynamic analysis of megawatt-scale high-speed machines for gas turbine applications, with particular attention to comparing 3-RAMB supported systems to conventional 2-RAMB configurations. The initial analysis examined whether adopting a 3-RAMB layout offers significant benefits over more conventional design.

Case R represents the most compact configuration, although it introduces assembly challenges, particularly with the shrink fitting of HPC 2 after part of other components have been installed. Case 1 is longer and heavier than Case R, also this shrink fitting of HPC 2 can be problematic as there is also coupling connection near. This coupling introduces minor complexities but also provides modularity, where this compressor part could be changed to other one if machine requirements sifts to other needs. Thermal side here extension shaft is between compressors and need heat shielding structure.

Case 4 most modular design as this can work with commercially available electric machine, but this modularity comes with assembly and thermal challenges. There is heavy turbine at other end and other end there is compressors where again this HPC 2 is needed to shrink fitted. There is also many components heating which needs shielding and cooling for other components as AMBs and TDB. Case 4 is also longest and heaviest design this extra bulkiness would be deterrent on some cases as it would need more room and robust installation platform.

From all cases Case R has the smallest footprint and is based on a more commercially available design, making it the most suitable choice for installations where size and cost are the primary constraints. However, if cost and size are not limiting factors and modularity is prioritized, then Case 4 becomes the preferred option due to its higher adaptability.

Case R presents uncertainties because accelerating machine to operational speed requires ig to go cross first FW bending mode which needs heavy damping from AMBs. At the same

time observability of this mode is limited. This affects machine controllability on start up and shutdown.

Case 1 demonstrates improved rotordynamic behavior, with maximum amplitude on first FW peak is one third from Case R, and observability is at similar level. However, this peak occurs near the lower end of the safety range and must still be crossed before reaching operational speed, which may pose challenges if damping is not applied effectively.

Case 4 exhibits lowest maximum amplitude of these cases being less than tenth of Case R maximum amplitude, providing the most favorable conditions for control machine in operation when this peak is crossed.

From a rotordynamic perspective, Case 4 is most suitable option, as it exhibits the lowest lateral amplitude at the first critical speed, reducing resonance risk and facilitating smoother crossing of this critical region. This characteristic enables more controlled acceleration and reduced vibration at operational speed. In all cases, the peak lateral amplitude at the RAMB sensor during the first FW bending mode is relatively similar, despite differences in machine speed, indicating consistent observability between cases.

In general, a 3-RAMB configuration can offer significant advantages when space constraints are not critical, modularity is desired, and an increase in the capital investment cost is acceptable. The additional bearing provides greater flexibility in the rotor layout and can simplify integration with electric machines or generators, potentially streamlining design for various applications and reducing production time. However, research on this configuration is still in its early stages and its adaptability in industrial settings remains uncertain.

Specifically, in this study, among all 3-RAMB design options, Case 4 demonstrated the most favorable dynamic performance, although its design introduces certain assembly and thermal challenges. This layout accommodates all process stages on a single extension shaft without requiring modifications to the electric machine rotor, thus enhancing modularity. From a rotordynamic perspective, Case 4 exhibited the lowest vibration levels, allowing easier crossing of the lower modes, including the first critical speed. Furthermore, the second forward-whirl critical speed is located well beyond the operational range approximately 90%

higher than the operational speed, minimizing vibration and significantly reducing the risk of resonance, even in overspeed conditions.

The purpose of this study was to evaluate the design and dynamic performance of megawatt-scale HS machines supported by 3-RAMB compared to the conventional 2-RAMB configuration. Future research should focus on validating these findings through experimental testing and prototype implementation to confirm the theoretical advantages identified, particularly in vibration control and resonance avoidance. Given its dynamic performance, Case 4 would be particularly interesting to investigate on moving platforms, where vibration control and stability are critical.

References

Bidaut, Y., R. Somaini & M. A. d. L. Ruguê. (2019). “TL04-Stability Considerations of Centrifugal Compressors Equipped with Active Magnetic Bearings.” In *Proceedings of the 48th Turbomachinery Symposium.* Turbomachinery Laboratory, Texas A&M Engineering Experiment Station, 2019. https://hdl.handle.net/1969.1/188639.

Breeze, P. (2016). *Gas-Turbine power generationran.* Academic Press, 2016.

Cengel, Y., & J. Cimbala. (2014). *Fluid mechanics fundamentals and applications.* McGraw Hill, 2014. ISBN: 978-0-07-338032-2.

Chen, W. J., & E. J. Gunter. (2001). *Introduction to dynamics of rotor-bearing systems.* 484. Concepts NREC, 2001. ISBN: 1-4120-5190-8.

Choudhury, T., J. Narsakka, K. M. Szombati, S. Madanzadeh, V. Abramenko, N. Nevaranta, H. Ebel, T.-T. Saaresti, J. Pyrhönen & J. Sopanen. (2025). “Multidisciplinary Design Approach for On-board High-speed Energy Conversion Machinery.” In *2025 IEEE International Electric Machines & Drives Conference (IEMDC),* 1057–1063. 2025. https://doi.org/10.1109/IEMDC60492.2025.11061157.

Choudhury, T., G. Ranjan, A. Smirnov, J. Heikkinen, L. Rauhala & J. Sopanen. (2024). “Effect of Labyrinth Seal Parameters on Leakage and Rotordynamics in a Centrifugal Compressor Supported by Active Magnetic Bearings.” In *Turbo Expo: Power for Land, Sea, and Air,* vol. 88025, V10AT22A016. American Society of Mechanical Engineers, 2024. https://doi.org/https://doi.org/10.1115/GT2024-126770.

Derakhshandeh, N. (2023). “Comparative rotor dynamic analysis of integrated and standalone compressors.” Master’s thesis, Lappeenranta-Lahti University of Technology LUT, 2023.

Genta, G. (2007). *Dynamics of rotating systems.* 674. Springer Science & Business Media, 2007. ISBN: 0-387-20936-0.

Gerada, D., A. Mebarki, N. L. Brown, C. Gerada, A. Cavagnino & A. Boglietti. (2013). "High-speed electrical machines: Technologies, trends, and developments." *IEEE transactions on industrial electronics* 61, no. 6 (2013): 2946–2959. https://doi.org/10.1109/TIE.2013.2286777.

Inman, D. J. (2014). *Engineering Vibration.* 4th. 720. Upper Saddle River NJ : Pearson Prentice Hall, 2014. ISBN: 0-13-287169-6.

Kang, M. S., & W. H. Yoon. (2005). "Acceleration feedforward control in active magnetic bearing system subject to base motion by filtered-X LMS algorithm." *IEEE Transactions on control systems technology* 14, no. 1 (2005): 134–140. https://doi.org/10.1109/TCST.2005.847337.

Kurvinen, E., T. Choudhury, J. Narsakka, I. Martikainen, J. Sopanen & R. P. Jastrzebski. (2021). "Design Space Method for Conceptual Design Exploration of High Speed Slitted Solid Induction Motor." In *2021 IEEE International Electric Machines & Drives Conference (IEMDC),* 1–8. 2021. https://doi.org/10.1109/IEMDC47953.2021.9449526.

Kurvinen, E., C. Di, I. Petrov, R. P. Jastrzebski, D. Kepsu & J. Pyrhönen. (2019). "Comparison of the performance of different asynchronous solid-rotor constructions in a megawatt-range high-speed induction motor." In *2019 IEEE International Electric Machines & Drives Conference (IEMDC),* 820–825. IEEE, 2019. https://doi.org/10.1109/IEMDC.2019.8785288.

Kutz, M. (2014). *Mechanical Engineers' Handbook, Volume 4 - Energy and Power (4th Edition).* John Wiley & Sons, 2014. ISBN: 978-1-118-11285-4. https://app.knovel.com/hotlink/toc/id:kpMEHVEPE1/mechanical-engineers/mechanical-engineers.

Lalanne, M., & G. Ferraris. (1998). *Rotordynamics prediction in engineering.* 252. John Wiley & Sons, 1998. ISBN: 978-0-471-97288-4.

Maslen, E. H., G. Schweitzer, H. Bleuler & M. Cole. (2009). *Magnetic bearings: theory, design, and application to rotating machinery.* Springer, 2009.

Matsushita, O., M. Tanaka, H. Kanki, M. Kobayashi & P. Keogh. (2017). *Basic rotordynamics: introduction to practical vibration analysis.* 367. Springer, 2017. ISBN: 9784431554554.

Moghaddam, R. R. (2014). "High speed operation of electrical machines, a review on technology, benefits and challenges." In *2014 IEEE Energy Conversion Congress and Exposition (ECCE),* 5539–5546. IEEE, 2014. https://doi.org/10.1109/ECCE.2014.6954160.

Narsakka, J., T. Choudhury, J. Sopanen, E. Kurvinen & J. Pyrhönen. (2023). "Effect of coupling stiffness on new high-speed electric machine driveline." In *2023 IEEE International Electric Machines & Drives Conference (IEMDC),* 1–7. IEEE, 2023. https://doi.org/10.1109/IEMDC55163.2023.10239033.

Rangwala, A. (2005). *Turbo-Machinery Dynamics: Design and Operation.* 535. New York: McGraw-Hill, 2005. ISBN: 0-07-145369-5.

Ranjan, G., J. Narsakka, T. Choudhury & J. Sopanen. (2023). "Dropdown Analysis of High-Speed Thin-Shaft Coupled Rotor System Integrated with Three Active Magnetic Bearings." In *International Conference on Rotor Dynamics,* 190–200. Springer, 2023. https://doi.org/https://doi.org/10.1007/978-3-031-40455-9_15.

Rowe, W. B. (2012). *Hydrostatic, Aerostatic and Hybrid Bearing Design.* Amsterdam : Elsevier, 2012. ISBN: 978-0-12-396994-1. https://ebookcentral.proquest.com/lib/lut/detail.action?docID=892249.

Smirnov, A., N. Uzhegov, T. Sillanpää, J. Pyrhönen & O. Pyrhönen. (2017). "High-Speed Electrical Machine with Active Magnetic Bearing System Optimization." *IEEE Transactions on Industrial Electronics* 64, no. 12 (2017): 9876–9885. https://doi.org/10.1109/TIE.2017.2716875.

Solar Turbines. (2019). *What are gas turbines and how do they work?* [Solar Turbines Website]. [Referenced 08-06-2025]. Available at: https://www.solarturbines.com/en_US/products/gas-turbines.html, 2019.

Sopanen, J. (2009). *Rotor-Bearing Dynamics Toolbox for Matlab Version 2.1.* LUT Machine Dynamics, Lappeenranta, Finland, 2009.

Sopanen, J. (2019). *RoBeDyn v.2.2 Theory Manual.* LUT Machine Dynamics, Lappeenranta, Finland, 2019.

Sultan, M. (2019). *What is a Gas Turbine?* [RealPars Website]. [Referenced 17-02-2025]. Available at: https://www.realpars.com/blog/gas-turbine, 2019.

Tenconi, A., S. Vaschetto & A. Vigliani. (2014). "Electrical Machines for High-Speed Applications: Design Considerations and Tradeoffs." *IEEE Transactions on Industrial Electronics* 61, no. 6 (2014): 3022–3029. https://doi.org/10.1109/TIE.2013.2276769.

Uzhegov, N., E. Kurvinen & J. Pyrhönen. (2014). "Design limitations of 6-slot 2-pole high-speed permanent Magnet Synchronous machines with Tooth-Coil windings." In *2014 16th European Conference on Power Electronics and Applications,* 1–7. 2014. https://doi.org/10.1109/EPE.2014.6910811.

Uzhegov, N., A. Smirnov, C. H. Park, J. H. Ahn, J. Heikkinen & J. Pyrhönen. (2017). "Design Aspects of High-Speed Electrical Machines With Active Magnetic Bearings for Compressor Applications." *IEEE Transactions on Industrial Electronics* 64, no. 11 (2017): 8427–8436. https://doi.org/10.1109/TIE.2017.2698408.

Van Millingen, R., & J. Van Millingen. (1991). "Phase shift torquemeters for gas turbine development and monitoring." In *Turbo Expo: Power for Land, Sea, and Air,* vol. 79023, V005T15A003. American Society of Mechanical Engineers, 1991. https://doi.org/https://doi.org/10.1115/91-GT-189.

Zhao, Y., P. Liu, Q. Lv, K. Zhang & L. Zhao. (2024). "Stability Assessment of the High-Speed Flywheel with AMBs on a Rotating Platform." *Energies* 17, no. 11 (2024). ISSN: 1996-1073. https : / / doi . org / 10 . 3390 / en17112746. https://www.mdpi.com/1996-1073/17/11/2746.